

Bayesian Optimisation of Large-Scale Biophysical Networks

J. Hadida^{a,b,*}, S.N.Sotiropoulos^{a,c},
R.G.Abeysuriya^b, M.W.Woolrich^{b,1}, S.Jbabdi^{a,1}

^a Wellcome Centre for Integrative Neuroimaging (FMRIB),
Nuffield Department of Clinical Neurosciences, University
of Oxford

^b Wellcome Centre for Integrative Neuroimaging (OHBA),
Department of Psychiatry, University of Oxford

^c Sir Peter Mansfield Imaging Centre (SPMIC), School of
Medicine, University of Nottingham

Abstract

The relationship between structure and function in the human brain is well established, but not yet well characterised. Large-scale biophysical models allow us to investigate this relationship, by leveraging structural information (*e.g.* derived from diffusion tractography) in order to couple dynamical models of local neuronal activity into networks of interacting regions distributed across the cortex. In practice however, these models are difficult to parametrise, and their simulation is often delicate and computationally expensive. This undermines the experimental aspect of scientific modelling, and stands in the way of comparing different parametrisations, network architectures, or models in general, with confidence. Here, we advocate the use of Bayesian optimisation for assessing the capabilities of biophysical network models, given a set of desired properties (*e.g.* band-specific functional connectivity); and in turn the use of this assessment as a principled basis for incremental modelling and model comparison. We adapt an optimisation method designed to cope with costly, high-dimensional, non-convex problems, and demonstrate its use and effectiveness. Using five parameters controlling key aspects of our model, we find that this method is able to converge to regions of high functional similarity with real MEG data, with very few samples given the number of parameters, without getting stuck in local extrema, and while building and exploiting a map of uncertainty defined smoothly across the parameter space. We compare the results obtained using different methods of structural connectivity estimation from diffusion tractography, and find that one method leads to better simulations.

Keywords: biophysical model, simulation, Bayesian optimisation, resting-state, diffusion, MEG

*Corresponding author

Email address: jhadida@fmrib.ox.ac.uk (J. Hadida)

¹Equal contribution

1. Introduction

Large-scale biophysical models (LSBMs) [60, 52, 4] offer a plausible mechanistic relationship between brain structure (anatomical properties) and function (dynamical properties). This relationship has previously been established by correlating anatomical connectivity (AC) with resting-state functional connectivity (FC) [32, 37, 44], leading to the hypothesis that resting-state activity is an emergent property of the brain, resulting from structured interactions between spatially distributed populations of neurons [19]. As such, it would be one of the few measurable forms of structure-function interaction at the macro-scale, and the ideal activity to compare against large-scale biophysical simulations.

Although the nature of these interactions remains to be characterised, this hypothesis is consistent with more functionally-oriented views, in which the brain is seen as a network of spatially segregated units, cooperating transiently over time in order to carry out the neural computations required for cognition [17, 26]. This view is generally accepted, but still poses many challenges (*e.g.* cortical parcellation, connectome estimation, multimodal integration), some of which affect the large-scale models that we study here. This should be kept in mind when discussing the results obtained with particular models, but the modelling approach itself remains relevant and attractive for many reasons.

Briefly, these reasons pertain either to a methodological, theoretical or clinical perspective. Methodologically, LSBMs offer a unified framework in which previously independent methods – such as diffusion tractography, neuronal population modelling and functional connectivity estimation – are allowed to interact. The ability to connect multiple aspects of brain structure and function via their dedicated fields of study is crucial if we are to build a coherent theory of brain activity. From a theoretical standpoint, these models are designed to provide a mechanistic summary of brain activity in terms of biologically interpretable parameters. A particular model then effectively encodes our understanding of some underlying process, at least to the extent that the empirical data can support. Finally, clinical considerations derive

from the theoretical ones; reliable estimates of biologically interpretable parameters can be used to characterise different conditions, or discriminate between them [62].

Here, we focus on the theoretical perspective; specifically with regards to the inference of model parameters from imaging data. Biophysical models typically describe the observed data (*e.g.* fMRI BOLD contrast or MEG) in terms of interpretable parameters (*e.g.* local balance of excitation and inhibition or the hemodynamic response). Because of this formulation, they are *generative* in nature: for a given set of parameters, one can easily generate synthetic data according to the model, which can then be compared to imaging data. However the reverse – estimating the parameters that best fit a given observation, also called *model inversion* – can be very difficult, depending on the number of parameters, the complexity of the model, and the amount of information in the observed data. Unfortunately in practice, empirical estimates of the model parameters are rarely available, and therefore model inversion is required in order to gain insight into the observed data. In this paper, we frame the inversion of LSBMs as an optimisation problem, propose a powerful method for solving this problem which can handle the computational burden usually associated with simulations, and demonstrate its effectiveness on a simple yet challenging example given the current state-of-the-art.

We model MEG resting-state data using delay networks of oscillatory neuronal masses, with five parameters controlling key structural and functional properties (*e.g.* average delay between brain regions or local frequency responses). This model is formulated mathematically as a large system of non-linear coupled delay-differential equations with over a hundred state-variables, which is numerically sensitive and computationally expensive to solve. To further add to the challenges, reliable estimations of functional connectivity patterns (which are compared against empirical measurements from MEG) require on the order of a minute worth of data, and numerical integration methods require timesteps below the millisecond. Therefore, exploring the different ways in which our model behaves as a function of the controlled parameters poses immediate difficulties in terms of computational tractability.

These circumstances call quite naturally for Bayesian optimisation methods; these methods operate under the assumption that the true objective function is computationally expensive to estimate, and instead proceed to *learning* it through iterative cycles of careful exploratory sampling and information consolidation. Specifically, the method presented in this paper is designed for high-dimensional (in practice up to a dozen parameters with typical LSBMs), non-convex and computationally costly problems [41]. It is able to explore the parameter space simultaneously at multiple scales, allowing local optima to compete for the best solution, and using uncertainty estimates to prioritize unexplored regions.

The remainder is organized as follows. We present the optimisation method in §2.1 and illustrate the algorithm on a toy-example in Fig. 2. We then introduce the LSBM used in our experiments in §2.2, and define the optimisation problem for model inversion (parameters and objective function) in §2.3. The data used in our experiments is described in §3.1, and implementation details are given in §3.2. Finally the results of our experiments are presented in §3.3 and discussed in §3.4.

2. Methods

2.1. Gaussian-Process Surrogate Optimisation

The method proposed is adapted from [41], and belongs to the family of Bayesian optimisation methods [6]. These methods are designed to tackle computationally expensive black-box global optimisation problems – that is, optimisation problems for which a global solution is sought, but where the objective function is expensive to evaluate, and analytics (*e.g.* the objective’s gradient) are not available. It is worth noting that this method is independent from the particular problem at hand, and may be applied to any other context with similar constraints.

In general, efficient optimisation methods exploit the structural properties of the problem (*e.g.* convexity) in order to devise a strategy which guarantees rapid convergence to a solution. But in the

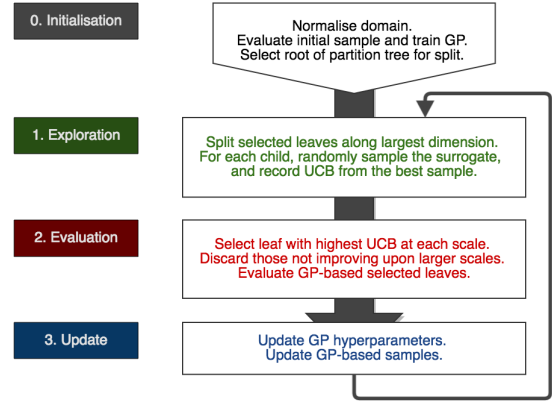


Figure 1: Algorithmic summary of Gaussian-Process Surrogate Optimisation (GPSO). The search space is initially rescaled to normalise the bounds in each dimension to $(0, 1)$. The iterations of the algorithm can be summarised in three main steps; **i)** *exploration*, where selected leaves are partitioned, and children are assessed using GP-UCB; **ii)** *evaluation*, where we evaluate leaves with maximal UCB at each scale, using the objective function; **iii)** *update*, where we re-train the GP including newly evaluated points.

case of black-box functions, these properties cannot be theoretically determined, and therefore an efficient strategy needs to discover them empirically and adapt as the optimisation progresses. Moreover in the case of expensive objective functions, the strategy needs to restrict the exploration of the search space to a minimum, in order to remain computationally tractable. This excludes in practice all strategies which rely on the gradient or Hessian (because numerical estimates require many function evaluations), but also stochastic sampling methods (*e.g.* MCMC, particle filters or genetic algorithms) which typically rely on large numbers of samples (either for diversity or statistical validity).

2.1.1. Optimism in the face of uncertainty

The problem of finding a suitable strategy given the previous constraints is best formulated within the framework of game theory, where computing-time is seen as a limited resource. The goal is to find the right balance between *exploring* the search space, in order to discover new places of interest with respect to the objective, and *exploiting* the knowledge accumulated by previous iterations, in order to prioritize a more detailed search in places of known inter-

est. This is known as the *exploration-exploitation dilemma*, the simplest instance of which is the so-called multi-armed bandit problem (MAB) [2].

In short, the MAB problem consists in picking iteratively from a finite set of possible choices, with repetitions allowed, where the outcome of each choice is random with unknown distribution. For any fixed number of picks, the goal is to maximise the cumulative outcome, by taking the best-known choice as often as possible (exploitation), while regularly trying out unknown or uncertain choices (exploration). A posteriori, the difference between the outcome achieved and the best possible outcome is called the *regret*; minimising the regret or maximising the reward is equivalent.

In this context, a successful balance between exploration and exploitation can be achieved by adopting an *optimistic* strategy, whereby at each turn, the best possible outcome for each choice is considered, given an estimate of uncertainty from previous trials. We then iteratively pick the choice with the best expected outcome, and update our uncertainty according to the result obtained. This strategy is known as the upper confidence-bound method (UCB), and in the next paragraphs we explain how it can be implemented in the context of non-linear optimisation. More detailed explanations about UCB can be found in [8].

2.1.2. Gaussian-Process surrogate

The previous paragraphs give an overview of the strategy adopted, but do not provide a practical solution to our problem. The first issue is that the MAB applies to finite sets of choices, whereas we consider search spaces in which each point is a candidate set of parameters for our models. In fact, adapting the UCB strategy to the latter goes even deeper than considering an uncountable set of choices, it also introduces the notion of a *neighbourhood* for each choice, which should be exploited to enforce smoothness assumptions and propagate knowledge about the objective.

The second issue concerns the representation of this knowledge. Bayesian optimisation methods are only able to tackle such difficult problems because

they effectively *learn* the objective as the optimisation progresses, and adapt their search for a solution according to the current state of belief at each iteration. This learned representation is typically defined smoothly across the search space, and much cheaper to evaluate than the true objective function. It can therefore be used as a *surrogate* for the true objective function during optimisation, allowing for computationally tractable analysis and exploration planning. To achieve this, a powerful mathematical tool is required; one not only capable of regressing any sample of points from the objective function (multivariate in general), but also providing smooth estimates of confidence (or uncertainty) across the search space.

Fortunately, this is exactly what Gaussian process regression (GPR) does, and it has been used successfully in the past to solve this second issue [15]. Moreover, resorting to Gaussian processes (GP) also provides intuition into the first issue; GPs can be thought of as an extension of multivariate Gaussian distributions to the infinite case, where any finite subset of points in the search space is itself Gaussian distributed, and the dependence between any pair of points is specified by the *covariance function*, which usually encodes the idea of neighbourhood (typically chosen as a decreasing function of the distance between two points). More details about GPs can be found in [49].

Using GPs enables the regression of any finite sample of points to represent arbitrary objective functions; provides us with a smooth estimate of uncertainty; and encodes the idea of neighbourhood explicitly via the covariance function. The only missing ingredient is a method to overcome the fact that points in the search space cannot be indexed like discrete choices (they are uncountable); without it, the present context of continuous optimisation cannot relate to the MAB problem, and the UCB strategy cannot be applied.

This is achieved in [41] by the introduction of a *partition function*, which splits the search space into distinct subregions that can be explored independently, and can in turn be partitioned themselves to reach a finer resolution – that is, the partition function is *recursive*. Recursivity confers exponential convergence towards regions of interest,

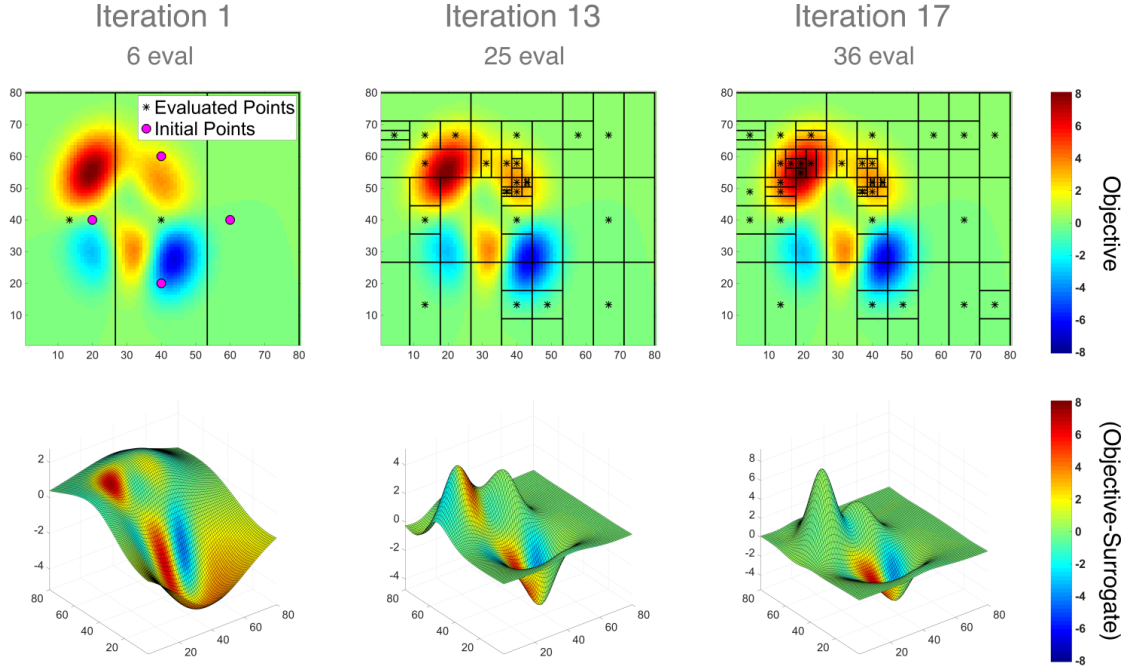


Figure 2: Gaussian-Process Surrogate Optimisation (GPSO) on Matlab’s **peaks** function. This figure shows the partition of the search-space overlaid on top of the true objective function (top-row), and surrogate objective function (bottom-row) for 3 different iterations (columns). Surfaces show the expected value of the GP surrogate, and colours indicate differences with the true objective: red tones mean the true objective is higher than the surrogate (conversely for blue). **Iteration 1.** Initial sample and 2 points evaluated in the first iteration; the top and bottom initial points are near a peak and a trough, hence the slope of the surrogate. **Iteration 13.** The algorithm initially finds a local maximum, and converges rapidly to its peak by refining the partition around it. Meanwhile, exploration at larger scales hits the slope of the highest peak; the surrogate function shows that the corresponding peak is misaligned (red patch between the two peaks), but it is already higher than the previous one. **Iteration 17.** The discovery of a higher peak at a larger scale froze the subdivision near the first local maximum. The algorithm converged to the global optimum after 4 iterations. The surrogate peaks are now both aligned with the truth (green colour).

and induces a hierarchical structure amongst sub-regions according to their size (larger regions are non-overlapping unions of the smaller regions contained within them), which can be represented by a *partition tree*. Each node in this tree corresponds to a rectangular region of the search space, covering a unique combination of subintervals in each dimension (each corresponding to a range of values for each parameter), and the size of which decreases strictly with the depth, allowing for arbitrarily high resolutions. In other words, the partition function allows us to identify regions in the search space with arbitrary resolution, and since there are only a discrete number of nodes at each level, the UCB strategy can be applied in a multi-scale fashion.

An illustration of this algorithm is presented in Fig. 2, using Matlab’s `peaks` function in a two-dimensional context. The partition of the search-space over three iterations is overlaid on top of the objective function (coloured background), to demonstrate the refinement of the resolution in places of interest. The associated partition tree is shown in Fig. 3, where each node corresponds to a different region of the search space (the deeper the node, the smaller the region), and colours indicate either the evaluated scores or the UCBs.

2.1.3. Concrete implementation

The main challenge of global optimisation methods, as opposed to local methods, is to deal with local extrema in the objective function. This challenge can be efficiently tackled by carrying out multiple local searches in a sequential (*e.g.* simulated annealing, Metropolis-Hastings) or parallel (*e.g.* particle filters, genetic algorithms) manner. The method proposed here implements a special case of the parallel approach, which organises candidate solutions hierarchically using the partition tree introduced in the last paragraph.

The algorithm proceeds iteratively (after initialisation) by: selecting *at each level* a leaf node with maximal UCB; subdividing selected leaves further using the partition function; exploring children nodes to assess their UCB; and retraining the GP surrogate with new evaluations of the objective function. We summarise this in the diagram Fig. 1. Note that, because selected nodes are leaves, we

consider at each step a set of regions located in different parts of the search space; and because we select at most one leaf per level in the partition tree, we explore the search space simultaneously at multiple scales.

From there, there are three points to clarify in order to get a concrete implementation:

1. For any point x in the search space, the upper-confidence bound is defined as:

$$\text{UCB}(x) = \mu(x) + \varsigma \sigma(x) \quad (1)$$

where $\mu(x)$ corresponds to the expected value of the objective function f at point x given by GPR, $\sigma(x)$ is the associated standard deviation, and ς is a positive factor controlling our optimism².

2. Each leaf node in the partition tree is labelled as being either: *evaluated*, meaning that the objective function was evaluated at its centre; or *GP-based*, meaning that its associated score was estimated by UCB. Specifically, the score associated with a GP-based leaf corresponds to the best UCB amongst N points randomly sampled within the corresponding area in the search space. At each iteration, selected GP-based leaves are evaluated prior to being partitioned, and the score associated with any evaluated node is the value of the objective function at its centre.
3. The partition function is a ternary split along the largest dimension of the subregion considered (in normalised coordinates). This is not a trivial choice; it satisfies several desirable properties with regards to the optimisation, although none of them is required. First, it produces non-overlapping subdivisions, which ensures that there is only one path converging to any specific point in the search space, avoiding redundant competition between nodes. Second, the centre of the parent node is also the centre of the middle child, which saves us an evaluation of the objective function at each split. And third, because of this conserved

²For a GP with Gaussian likelihood kernel, the upper bound of a $p\%$ confidence interval on the expected value corresponds to $\varsigma = \text{erfc}^{-1}(p/100)$, where erfc is the complementary Gauss error function.

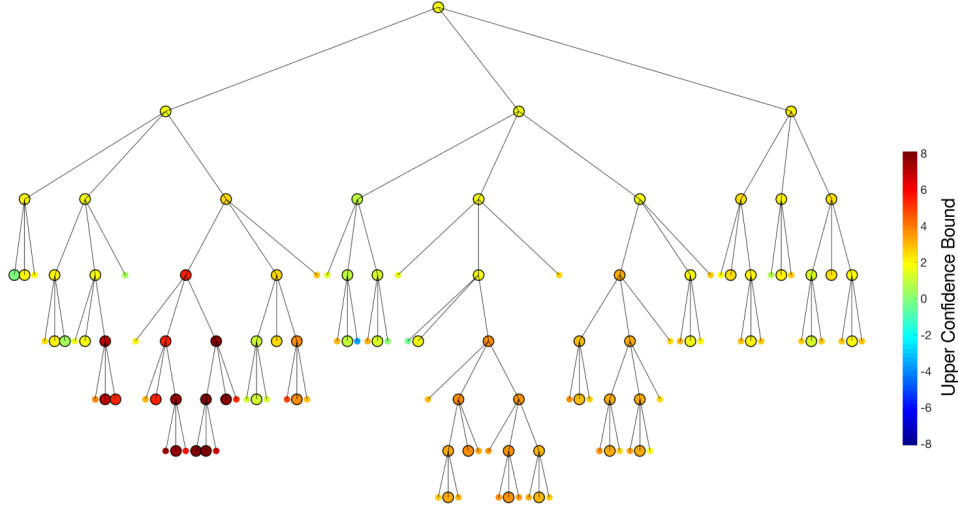


Figure 3: Ternary partition tree associated with the example shown in Fig. 2. Each node corresponds to a different subinterval of the search space; colours correspond to the associated scores (upper-confidence bounds); and edges represent set-inclusion (parent intervals are the union of their children). In particular, deeper nodes correspond to smaller intervals in the search-space (resolution increases with the depth). Bigger nodes with a black rim indicate that the objective function was evaluated at their centre, smaller nodes were assessed using the GP surrogate only. Deeper orange branches at the centre correspond to the local maximum found initially, and red branches on the left correspond to the highest peak.

point, we can guarantee that the children of a node do not recede, meaning that the progression within a branch is monotonic.

Finally, an improvement can be made on the selection process; it is pointless to explore regions at a smaller scale, if some region at a larger scale has a better expected score. Therefore, the selection proceeds sequentially from the root to the deeper branches, and we discard levels at which the maximum UCB does not improve upon the best expected score so far. In effect, this introduces competition between the different scales, and prevents dwelling around local extrema.

The benefits of this improvement are illustrated in Fig. 2, where the exploration of the first local extremum stops after a region at a larger scale obtains a better score. This exploration will only resume once all regions at the same resolution are either explored (unlikely) or obtain a lower expected score than this local extremum. Further evidence of the ability of GPSO to converge towards the global optimum will be presented in the context of LSBM optimisation (see Fig. 7), and in higher-dimensional spaces (see appendix).

2.2. Large-Scale Biophysical Model

In this paper, we use the Bayesian optimisation approach introduced in the previous section in order to optimise the parameters of whole-brain dynamical models. Specifically, we consider networks of interacting Wilson-Cowan oscillators with delays. This model posits that the electrophysiological oscillations typically observed in MEG data result from cycles of excitation and inhibition [61], and has been employed previously, notably in [16] to highlight the importance of propagation delays and long-range couplings between distant brain regions, with regards to synchronisation properties in the dynamics produced.

2.2.1. Assumptions and definitions

The brain is modelled as a network of neuronal masses, in which *vertices* correspond to spatially-contiguous brain regions, and *edges* represent direct interactions between these regions. Each neuronal mass may contain several subpopulations of neurons, or several state equations, and so to distinguish between these local entities and the different brain regions in the network, we call *nodes* the

Symbol	Description	Value
τ	Time-constant	10 ms
μ	Response threshold	3
σ	Dynamic range	$\mu/6$
c_{ee}, c_{ei}	Excitatory coupling	28, 7
c_{ie}, c_{ii}	Inhibitory coupling	-35, 0
P_i	Inhibitory input	-0.3

Table 1: Baseline parameters for the Wilson-Cowan model (see Eq. 3,4). Where subscripts are omitted, the description and value of the parameter apply to both subpopulations. The excitatory input P_e is controlled during our experiments. The response parameters (μ, σ) were set such that small inputs (compared to the dynamic range) would cause the system to oscillate. The couplings were set according to a ratio of 80% self-excitation ($c_{ee}/(c_{ee} + c_{ei}) = 0.8$), and such that the relative strength of excitation and inhibition would be equal ($c_{ee} + c_{ei} = c_{ie} + c_{ii}$).

vertices corresponding to a subpopulation or state equation, and *units* the groups of vertices located in the same brain region.

We are interested in emergent oscillatory activity in these networks, which is assumed to be driven by cycles of excitation and inhibition in each region. Therefore, two subpopulations of neurons are considered: an *excitatory* subpopulation (E) driving towards increased oscillatory activity, and an *inhibitory* subpopulation (I) driving towards quiescence. The effects of self- and long-range inhibition are neglected, meaning that there are no I-to-I edges, and only E-to-E edges between units. Finally, we do not consider noisy inputs or synaptic plasticity in this paper: their effects has been explored in separate work [1].

2.2.2. Local oscillations

The Wilson-Cowan model [61] (henceforth W-C) describes the temporal variations of the amount of neurons firing within an excitatory and an inhibitory population of neurons, given static local couplings between the two (related to the distribution of synaptic connections), and an external input controlling the excitability of the system.

It introduces so-called “subpopulation response functions”, defined as the cumulative distribution

of local firing-thresholds within each subpopulation. These distributions are generally assumed unimodal and symmetric, leading to sigmoidal cumulative functions. In practical terms, the subpopulation response function represents the expected response of an initially quiescent population of neurons to an external input, and is modelled as a logistic sigmoid:

$$\forall x \in \mathbb{R}, \mathcal{S}(x; \mu, \sigma) = \frac{1}{1 + e^{-\hat{x}}} \quad \hat{x} = \frac{x - \mu}{\sigma} \quad (2)$$

where μ represents the response threshold, and σ controls the width of the dynamic input range.

Let $E(t)$ denote the ratio of excitatory neurons firing at time t within a brain region (resp. $I(t)$ for inhibitory neurons). Neglecting refractory effects, the W-C model states that:

$$\tau_e \partial_t E = -E + \mathcal{S}_e(c_{ee}E + c_{ie}I + P_e) \quad (3)$$

$$\tau_i \partial_t I = -I + \mathcal{S}_i(c_{ei}E + c_{ii}I + P_i) \quad (4)$$

where $\partial_t \bullet$ denotes the derivative with respect to time; $c_{xy} \equiv c_{x \rightarrow y}$ is the directional coupling of x affecting y ; $\mathcal{S}_{e,i}$ are the subpopulation response functions; and $P_{e,i}$ are external inputs. The remaining parameters are given in Tab. 1. Notice that although the equations are identical for both subpopulations, the inhibitory coupling coefficients c_{ie} and c_{ii} must be non-positive (by definition), while the excitatory coefficients c_{ee} and c_{ei} must be positive, which breaks the apparent symmetry between excitation and inhibition.

In summary, the oscillatory mechanism of this model is simple: i) excitatory inputs lead to an increase in excitatory activity; ii) excitatory activity causes an inhibitory response; iii) decreased excitation leads to decreased inhibition; iv) which, in turn, leads to a relative increase of excitatory inputs. The architecture of this model, as well as typical dynamics produced, and the effects of key local parameters on these dynamics, are shown in Fig. 4.

2.2.3. Network extension

Extending the previous local equations to a network of interacting brain regions consists in adding

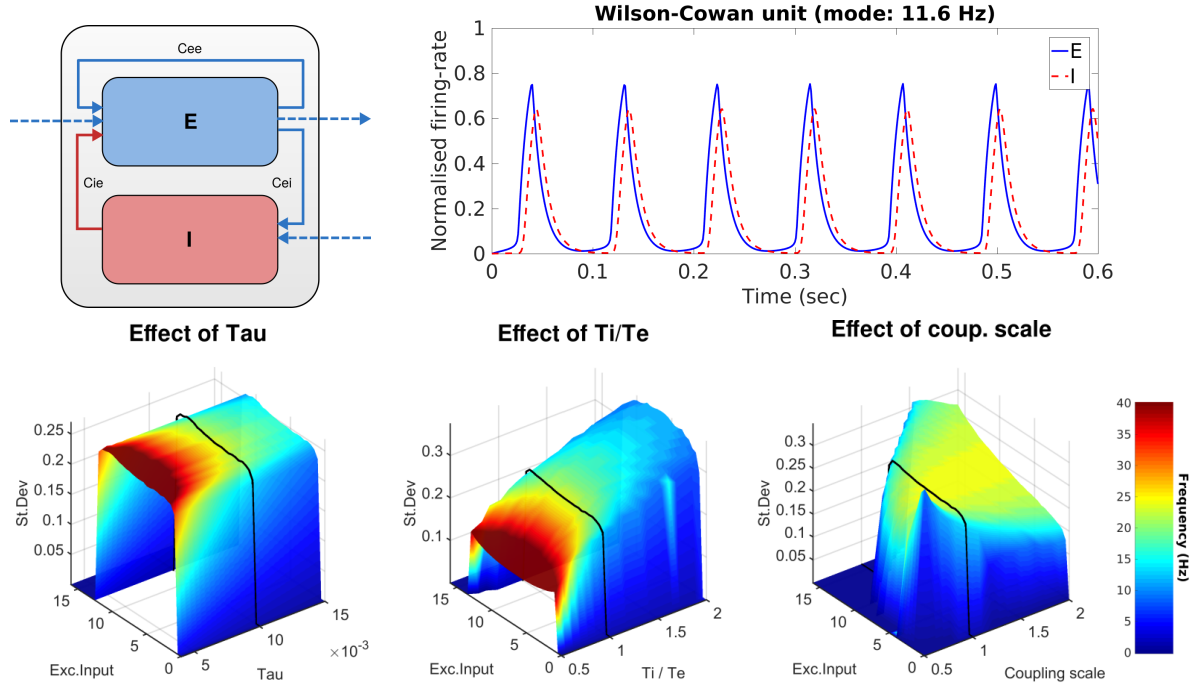


Figure 4: Illustrations of the Wilson-Cowan unit. **Top-left:** local two-population structure (excitatory and inhibitory), without self-inhibition ($c_{ii} = 0$) and with long-range excitation only (blue dashed lines). **Top-right:** example oscillatory timecourse showing inhibition (red dashed line) lagging behind excitation (blue plain line); the lag is controlled by the decay-times $\tau_{e,i}$, and here $P_e = 0.84$. **Bottom-row:** evolution of standard-deviation (surface height) and frequency mode (colormap) as a function of excitatory input, and varying parameters. Black lines correspond to increasing P_e , using baseline parameters given in Tab. 1. The unit is always silent without excitatory input, and saturates for large inputs – the interval between oscillatory and saturation thresholds is the *dynamic range* of the unit. Notice that the frequency of oscillations depends on the input; this property allows remote brain regions to affect the local phase via their connection, which is a potential mechanism for long-range synchronisation. *Left:* the oscillatory frequency can be controlled by shifting both time-constants $\tau_{e,i}$ simultaneously. *Middle:* controlling τ_i with τ_e fixed affects *both* the frequency and amplitude of the oscillations. *Right:* an upscale of local couplings dilates proportionally the dynamic range of the unit.

coupling terms from those remote regions inside the subpopulation response functions. The general *node* equation (whether excitatory or inhibitory) in a network of N brain *units* is therefore:

$$\tau_k \partial_t X_k = -X_k + \mathcal{S}_k \left(\sum_{j=1}^{2N} c_{j,k} X_j(t - \lambda_{j,k}) + P_k \right) \quad (5)$$

where $1 \leq k \leq 2N$ with the convention that odd indices correspond to excitatory nodes (resp. even for inhibitory nodes); X_k is the normalised firing-rate of node k (corresponding to previous variables E and I at the unit-level); and we introduced delay parameters $\lambda_{j,k} \equiv \lambda_{j \rightarrow k} \in \mathbb{R}_+$ to account for propagation times between distant brain regions. These delays are of the same order of magnitude as the decay-times of local subpopulations, and therefore interfere with their dynamics³.

2.3. Model Optimisation

The model presented in the previous section describes the activity of a network of N brain regions, using $2N$ state equations (see Eq. 5). In general, this network will not be sparse, meaning that there are $\mathcal{O}(N)$ non-zero coupling terms in most state equations, hence the high computational costs associated with simulations in practice (there are $\mathcal{O}(N^2)$ interaction terms to be computed at each time-step). As it stands, there are also $\mathcal{O}(N^2)$ parameters, because of the coupling and delay matrices, respectively $[c_{i,j}]$ and $[\lambda_{i,j}]$. It is therefore impractical to move on directly to the simulation of such systems, without a more parsimonious parametrisation of the model.

In this section, we propose a simple parametrisation controlling key structural and functional aspects of the system with few parameters. These parameters can be inferred from empirical MEG data, using the method presented previously in §2.1, by framing model inversion as an optimisation problem, for which we propose an objective function below.

³Such delays are caused mainly by axonal conduction and synaptic transmission, both highly dependent on temperature, and range from hundreds of micro-seconds to tens of milli-seconds at long-range [51].

2.3.1. Assumptions

For simplicity, we assume that all units in the network are identical, and that excitatory and inhibitory subpopulation response functions and time-constants are identical (see Tab. 1 for baseline parameters). Each unit is normally defined by 9 parameters (τ, μ, σ for each node, and c_{ee}, c_{ei}, c_{ie}), so these assumptions reduce the number of unit parameters from $9N$ to 6.

Since there are two nodes per unit (excitatory and inhibitory), the connectivity and delay matrices have a 2-block structure. For instance, with the coupling matrix, all on-diagonal blocks are identical (and contain the local couplings), and off-diagonal blocks only have one non-zero entry (only E-E long-range connections):

$$\underbrace{\begin{pmatrix} c_{ee} & c_{ei} \\ c_{ie} & 0 \end{pmatrix}}_{\text{On-diagonal}} \quad \underbrace{\begin{pmatrix} c_{i,j} & 0 \\ 0 & 0 \end{pmatrix}}_{\text{Off-diagonal}}$$

With the delay matrix, we reason in pairs of units instead of nodes (*i.e.* the delay between two regions is the same regardless of which subpopulations we consider in each). Therefore the 2-block between units i and j is simply:

$$\lambda_{i,j} \begin{pmatrix} 1 & 1 \\ 1 & 1 \end{pmatrix}$$

and we neglect delays within units ($\lambda_{i,i} = 0$). Delays are estimated from pairwise Euclidean distances, and we assume a constant propagation velocity throughout the brain to avoid introducing additional parameters.

We only consider cortico-cortical connections in this work, and assume that the two hemispheres correspond to subnetworks of equal size ($N/2$ units). The latter induces an additional N-block structure in the previous matrices, which is useful for two reasons:

- to our knowledge, there is no evidence for one hemisphere driving brain activity more than the other, or for a lateral bias in the AC between hemispheres, therefore requiring both to have the same size ensures that the overall AC within and between hemispheres is structurally unbiased;

- from a purely practical perspective, the assumption of hemispheric symmetry makes it easier to manipulate connections within and between them, as in Eq. 8 for instance.

Finally, note that despite these numerous assumptions the network is still heterogeneous due to the different coupling weights and delays assigned to the edges of the network; this is consistent with the overall objective of studying the effects of structural properties on dynamical activity.

2.3.2. Parametrisation

Let D be the matrix of pairwise Euclidean distances between brain regions, and A the associated matrix of anatomical connectivity estimated from diffusion tractography (both $N \times N$). By convention, the diagonal of A is set to zero, and we recall that excitatory and inhibitory nodes are indexed between 1 and $2N$, respectively with odd and even numbers.

The coupling matrix $C = [c_{i,j}]$ and delay matrix $\Lambda = [\lambda_{i,j}]$ are parametrised respectively as follows:

$$C = \underbrace{\gamma A \otimes \begin{pmatrix} 1 & 0 \\ 0 & 0 \end{pmatrix}}_{\text{non-local}} + \underbrace{I_N \otimes \begin{pmatrix} c_{ee} & c_{ei} \\ c_{ie} & 0 \end{pmatrix}}_{\text{local}} \quad (6)$$

$$\Lambda = \frac{\bar{\lambda}}{\bar{D}} D \otimes \begin{pmatrix} 1 & 1 \\ 1 & 1 \end{pmatrix} \quad (7)$$

where \otimes is the Kronecker product; I the identity matrix; \bar{D} the average pairwise distance; and we introduced the following parameters:

- γ the global coupling strength, controlling the overall amount of non-local coupling;
- and $\bar{\lambda}$ the average propagation delay, controlling the speed of interactions.

Note that although matrix A might be symmetric, C is *not*; the element in row i column j corresponds to the edge from node i to node j (not unit), and therefore each column can be seen as a coupling vector for the corresponding node.

Probabilistic tractography methods have an inherent bias towards shorter connections; longer

streamlines are less probable, and therefore connectivity between distant regions is generally lower [55] (see Fig. 5). This may reflect a biological reality [22], but beyond the issue of assessing the accuracy of the estimated decrease, there is the question of whether the same decrease rates apply equally within or between hemispheres. In order to correct for such potential bias, we introduce an additional parameter h to manually scale inter-hemispheric connections, which correspond to the off-diagonal N-blocks in matrix C . This scaling is affected to A directly, before substitution in Eq. 6:

$$A \leftarrow A \odot \left[\mathbf{1}_{N/2} \otimes \begin{pmatrix} 1 & h \\ h & 1 \end{pmatrix} \right] \quad (8)$$

where \odot is the Hadamard product (element-wise) and $\mathbf{1}$ is a full matrix of ones.

Finally, we consider two functional parameters affecting the oscillatory dynamics of all units:

- the time-constant τ , assumed equal for all nodes, which controls the frequency response of W-C units (see Fig. 4);
- and the excitatory input P_e , assigned equally to all excitatory nodes in the network, which controls the *excitability* of individual units when they are below oscillatory threshold.

Equations 6, 7 and 8 determine entirely the network structure, and we consider *five parameters* to be optimised, in Tab. 2, which control key structural and functional aspects of our model.

2.3.3. Relative variants

The previous parameters control key structural and functional aspects of our LSBM, but their range of values can vary depending on the AC matrix considered (and more generally, the oscillatory unit considered). This means that a suitable domain for optimisation needs to be determined *ad hoc* every time, which makes it difficult to compare solutions found across models.

We know (see Fig. 4) that W-C units oscillate for excitatory inputs beyond a certain threshold value P_e^* . Similarly at the network level, we know that

Symbol	Description	Short-name	Range
\widetilde{P}_e	Relative input	Input	(0.6, 1)
$\widetilde{\gamma}$	Relative coupling	Coupling	(1, 3)
$\bar{\lambda}$	Average delay (ms)	Delay	(1, 50)
h	Inter-hem. scaling	IH Scaling	(0, 4)
τ	Time-constants (ms)	Tau	(4, 16)

Table 2: Network parameters controlled during optimisation. The ranges correspond to the boundaries of the search space (required by GPSO). The parameter variants \widetilde{P}_e and $\widetilde{\gamma}$ are defined in §2.3.3. Short names are used in figures 7, 10 and 12.

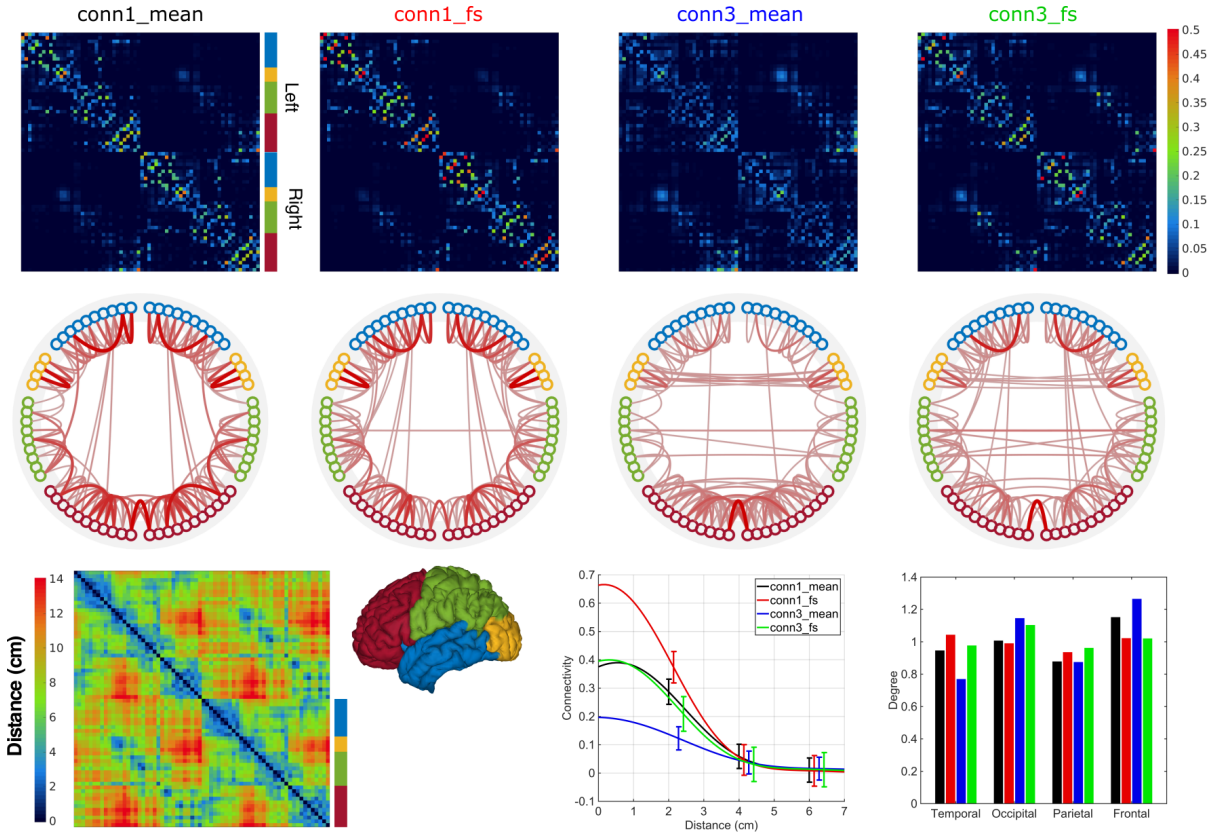


Figure 5: Structural information used in the biophysical models. **Row 1:** AC matrices estimated from diffusion tractography, using two different seeding methods (conn1, conn3), and two normalisation methods (mean, fractional scaling), see §3.1.1 for details. **Row 2:** thresholded network (90th percentile) showing the strongest edges in corresponding AC matrices. **conn3** seeding favours homotopic connections, whereas **conn1** favours anterior-posterior connections, and **mean** normalisation shows stronger connectivity in the frontal lobe. **Bottom-left:** matrix of pairwise distances showing hemispheric block structure. Lower distances around the diagonal are due to the ordering of the different regions (chosen manually). **Bottom-right:** basic statistics on connectivity weights. Connectivity decreases exponentially with the distance (left, GP regression showing predicted means and 95% confidence intervals). Average degrees are higher in the frontal and occipital lobes (right, bars shown for each method, and grouped by lobe); fractional scaling reduces frontal connectivity, while increasing temporal and and parietal ones; and **conn1** seeding yields higher connectivity in the temporal lobe, and lower in the occipital lobe.

oscillations occur for coupling values beyond a certain threshold value γ^* (which is null if the units intrinsically oscillate on their own).

Normalising these parameters with respect to their threshold value would help, not only to compare them across different models, but also to easily control the state of the network (oscillating or silent) and focus on the oscillating regimes during optimisation. Hence, we define the following *relative* variants instead:

$$\widetilde{P}_e = P_e/P_e^* \quad \widetilde{\gamma} = \gamma/\gamma^* \quad (9)$$

and use them throughout our experiments.

With these definitions, we know for example that $\widetilde{P}_e < 1$ corresponds to brain units below oscillatory threshold, and that networks are in oscillatory regime only when $\widetilde{\gamma} > 1$. And we can enforce these conditions during optimisation by choosing the parameter ranges accordingly (see Tab. 2).

However, determining the threshold value γ^* is not trivial, because it depends on P_e^* (the unit oscillatory threshold), as well as on other controlled parameters such as the average delay and inter-hemispheric scaling. While P_e^* can be determined numerically (*e.g.* with bifurcation analysis), to our knowledge there is no simple method for estimating the oscillatory coupling threshold γ^* for any given delay-network.

In our experiments, for any candidate set of parameters (including normalised input and coupling), both threshold values were estimated prior to simulation in order to determine the corresponding values P_e and γ , which are required in order to build the network (see previous section). This was done by dichotomic search with a precision of 3 significant digits. The overhead introduced, in terms of runtime, was on the order of a minute per candidate set of parameters (largely dominated by the search for γ^* ; the search for P_e^* always took less than a second).

2.3.4. Objective function

The *optimal* parameters should maximise the similarity between biophysical simulations and real

MEG data, and this similarity should be assessed using characteristic features of resting-state dynamics. In this paper, we take a simple objective function comparing FC matrices across six overlapping frequency bands:

$$[4, 8] [6, 10] [8, 13] [10, 20] [13, 30] [20, 40] \text{ Hz}$$

As excitatory pyramidal cells contribute most strongly to EEG/MEG signals, we associate activity in the excitatory populations of the model with signals in experimental data [9]. Envelope correlations were computed in each band, as is commonly done with resting-state MEG (more details in §3.1.2).

Importantly, the simulated timeseries were orthogonalised prior to computing Hilbert envelopes (using the Procrustes method from [12]), in order to replicate the effects of leakage correction on source-reconstructed MEG data.

Denoting $M_{1..6}$ the corresponding FC matrices, where subscripts identify the frequency-band, we define the *relative connectivity magnitude* as:

$$\mathbf{u} = \left[\frac{\mu_k}{\max_b |\mu_b|} \right]_{k=1..6} \quad (10)$$

where μ_b is the average off-diagonal correlation coefficient in matrix M_b . By definition, the largest element in this vector has magnitude 1 (*e.g.* in alpha band), and the other values give the relative amount of connectivity in one band compared to the principal one (*e.g.* in theta compared to alpha).

This vector is computed for the simulated and reference data independently, in order to compare the relative amounts of connectivity across frequency bands. Note that because we divide by the largest correlation coefficient across bands, this comparison is insensitive to any scaling of either set of matrices (reference or simulated), which can vary as a function of the signal-to-noise ratio for instance, or the amplitude of the oscillations.

Finally, the objective function used in our experiments combines the similarity between relative connectivity magnitudes, and the average within-band

correlation between simulated and reference FC matrices:

$$\left[1 - \text{RMS} \left(\frac{\mathbf{u}^{\text{ref}} - \mathbf{u}^{\text{sim}}}{2} \right)\right] \cdot \frac{1}{6} \sum_{b=1}^6 \text{Corr}(M_b^{\text{sim}}, M_b^{\text{ref}})$$

where superscripts refer to the simulated or reference data, and the first factor is a normalised measure of similarity (in $[0, 1]$) based on a root-mean-square metric, which is 1 when $\mathbf{u}^{\text{ref}} = \mathbf{u}^{\text{sim}}$, and decreases towards 0 as the distance between them increases.

3. Results & Discussion

3.1. Imaging data

3.1.1. Anatomical structure

The Desikan-Killiany cortical parcellation [20] was used in all experiments to define brain regions (or “units” in our network models). The AC between regions was estimated using probabilistic diffusion tractography [3, 39], and averaged across 10 diffusion MRI datasets from the Human Connectome Project (HCP) [59, 54]. Distortion corrected data [30] was used to estimate fibre orientations [40, 36], and used subsequently for probabilistic tractography in FSL. Delays between regions were estimated using Euclidean distances between the region’s barycentres.

Two different seeding methods were used to compute dense tractography connectomes: with the `conn1` method, streamlines were seeded from the WM/GM interface; whereas the `conn3` method considered every brain voxel as a seed. The number of streamlines reaching locations on the WM/GM boundary ($\sim 60\text{k}$ vertices in standard MNI space, as given by the CIFTI format [30]) were recorded.

Both connectomes were then parcellated and normalised in order to estimate anatomical connectivity between each region. Two different normalisation methods were used [22]:

- the **mean** method counts the number of streamlines between pairs of vertices belonging to two regions, and divides by the number of vertices in both;

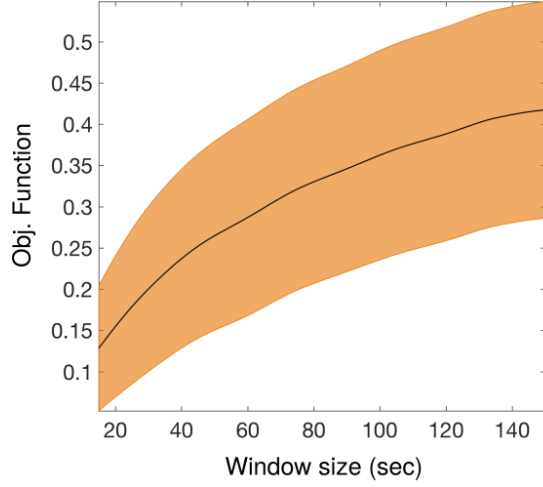


Figure 6: Distribution of similarity score (see §2.3.4) estimated on real MEG data across all 28 subjects, for time-windows of varying length (15 to 150 sec, 50% overlap). The black centreline is the median similarity score as a function of the window-length, and the orange patch shows the associated 95% confidence interval. This distribution is used as a gold-standard to assess the performance of our simulations; for a time-length of 60 sec, the upper similarity bound with 95% confidence is 0.41, and the best score obtained with our simulations was 0.42 (see Fig. 11).

- whereas fractional scaling (**fs**) divides instead by the sum of all streamlines involving either of two regions.

Conceptually, the first normalisation accounts for differences in *size* between different regions, while the second method accounts for differences in *connectivity* between pairs of regions instead (which indirectly accounts for differences in size as well).

Finally, each connectivity matrix was made symmetric by arithmetic average with its transpose, and rescaled such that the average degree (sum of rows or columns) be unitary. The corresponding AC matrices are shown in Fig. 5.

3.1.2. MEG resting-state

The resting-state datasets of 28 healthy subjects from previous studies [7, 50] was used in our experiments. Details about the acquisition and pre-processing can be found in these references. In particular, the anatomy of the subjects was aligned

with the MEG sensor-array by a combination of head-tracking (using fiducial coils), and surface-matching between a digitised head-shape and one derived from structural MRI, as is common for MEG acquisitions. The data were beamformed into MNI 8mm standard space between 4 and 40Hz, parcellated using PCA, rescaled to set the largest standard-deviation to 1, and orthogonalised to correct for spatial leakage using the Procrustes method from [12].

Each dataset was then filtered in the following six overlapping frequency bands:

[4, 8] [6, 10] [8, 13] [10, 20] [13, 30] [20, 40] Hz

and correlations between Hilbert envelopes were computed in each band. The resulting band-specific FC matrices were then averaged across 28 subjects, and taken as *reference data* for our simulations to be compared against. These reference FC matrices in theta, alpha and beta bands are shown along with the best simulated results in Fig. 9.

In addition, we performed a time-windowed analysis on real MEG data in order to assess the best similarity scores to be expected as a function of the simulation time-span in our experiments (see objective function in §2.3.4). Specifically, for a window of a given time-length, we extracted segments of source-reconstructed time-series from all 28 MEG datasets, estimated the functional connectivity matrices for each of these segments, and computed the associated similarity scores as if those were simulated data.

The distribution of scores obtained (see Fig. 6) was taken as a gold-standard for our simulations; we should expect our best simulations to hit the upper-end of this distribution, but significantly higher scores would indicate overfitting, and lower scores would indicate poor model performance.

We also used this analysis in order to strike a reasonable balance between higher expected scores and longer simulation times. The computational costs associated with longer simulations were considerable, and this analysis allowed us to assess the expected penalty for choosing shorter simulation times. We opted for simulations with an equivalent of 60 seconds worth of data in our experiments

(downsampled to 300 Hz before analysis); for this time-length, the corresponding upper-bound for the expected similarity scores with 95% confidence is 0.41, and the best score obtained in our experiments was 0.42 (see Fig. 11).

3.2. Software implementation

3.2.1. GP Surrogate Optimisation (GPSO)

We improved upon the implementation of IMGPO [41], by addressing a number of issues and extending the algorithm in several ways. Our implementation is a complete refactoring of the original algorithm, and is made freely available⁴.

Our main contributions are listed below:

- to update upper-confidence bounds following the optimisation of GP hyperparameters at each iteration, in order to allow belief propagation across the partition tree;
- to enable the exploration of candidate leaves using uniformly random samples of points in the corresponding subregion of the search-space (the original implementation only explored a subset of the dimensions in a deterministic manner);
- to implement serialisation, allowing for the optimisation to be resumed at any stage.

The various settings used during our experiments are listed in Tab. 3.

3.2.2. Biophysical Simulations

The LSBM presented in §2.2 was implemented in C++, and simulations were analysed with Matlab. The system of non-linear coupled delay-differential equations (see Eq. 5) was solved using an adaptive-step Runge-Kutta method of order 8 adapted from the reference Fortran implementation `Dopr853` in

⁴See: <https://github.com/jhadida/gpso>. The license (AGPLv3) permits any use of the code, without warranty, provided that license and contributors are preserved, and that any modification is made freely available under the same terms.

Function	Hyperparameter	Value
UCB	ς	1.98
Constant mean	μ	0
Gaussian likelihood	σ	0.001
Isotropic Matérn covariance (order 5)	Length	0.25
	Magnitude	1

Table 3: GPSO hyperparameters and initial values used for all experiments. The optimism ς corresponds to confidence bounds of 99.5% (*i.e.* $\text{erfc}^{-1}(0.005)$), which was found to strike a good balance between exploration and exploitation.

[33]. The main computational bottleneck in the simulations is due to the number of feedback terms to be computed at each time-step; since network matrices (delay and coupling) are not sparse, the complexity is quadratic in the number of nodes in the network. At each timestep of size h , the sum of delayed terms in each equation were computed across multiple threads at time t and $t + h$, and interpolated for each substep using an exact formula (that is, the interpolation does not make any approximation). These optimisations allowed for simulation times roughly two times slower than real-time using four threads on modern CPUs.

The initialisation of delay-systems is a sensitive operation. In contrast with initial-value problems, which typically require a single initial state, delay-systems require a smooth *function* for initialisation. This function must be defined over a time-interval $[t_0 - \lambda, t_0]$, where t_0 is the initial time and λ is at least as large as the largest delay. Additionally, it should itself be a solution of the system, which makes the problem circular.

To our knowledge, there is no solution to this problem. In our experiments, for each simulation, we calculated the fixed point (E, I) to which individual units converged given the current excitatory input⁵, and set the initial function to be constant and equal to these values in each unit. It is equivalent to assume that units are initially disconnected from the network for a certain period of time.

⁵We know it is a fixed-point because we only choose inputs below oscillatory threshold (see Tab. 2).

3.3. Experiments

We present the results of two experiments which demonstrate the benefits of GPSO in the context of LSBMs. The first experiment is a proof of concept in a restricted two-dimensional case, which allows results to be visualised and compared with exhaustive search. The second experiment considers the full model with five parameters, for which we provide a detailed analysis of the results and highlight the current limitations.

3.3.1. Two-dimensional example

In this experiment, the similarity between simulated and reference MEG data was maximised according to the objective function defined in §2.3.4, by optimising just two parameters for now; the average delay $\bar{\lambda}$, and the relative network coupling $\tilde{\gamma}$. The remaining parameters (see Tab. 2) were set to: $\bar{P}_e = 0.85$, $h = 1$, $\tau = 10\text{ms}$, and we used the `conn1_mean` AC matrix to connect the network units. The timespan of each simulation was 63 seconds, and we discarded the first 3 seconds to get rid of transient effects before analysis. The results are shown in Fig. 7.

The performance of GPSO was assessed by comparison with an exhaustive grid search, which is computationally tractable with two dimensions and can be easily visualised. The grid search required 525 simulations, considering respectively 25 and 21 equally spaced points across the value ranges of the delay and coupling parameters. In comparison, GPSO was run with 100 simulations, with which it successfully converged to the optimum, while learning a surrogate objective function defined smoothly across the search space, along with a map of uncertainty. These results demonstrate the efficiency of the method in a restricted two-dimensional context of LSBM optimisation. The performance of GPSO in higher dimensions is further assessed in the appendix, where we also provide a comparison with particle-filter optimisation [42].

3.3.2. Five-dimensional analysis

In this second experiment, we consider all five parameters listed in Tab. 2, and all four connectivity

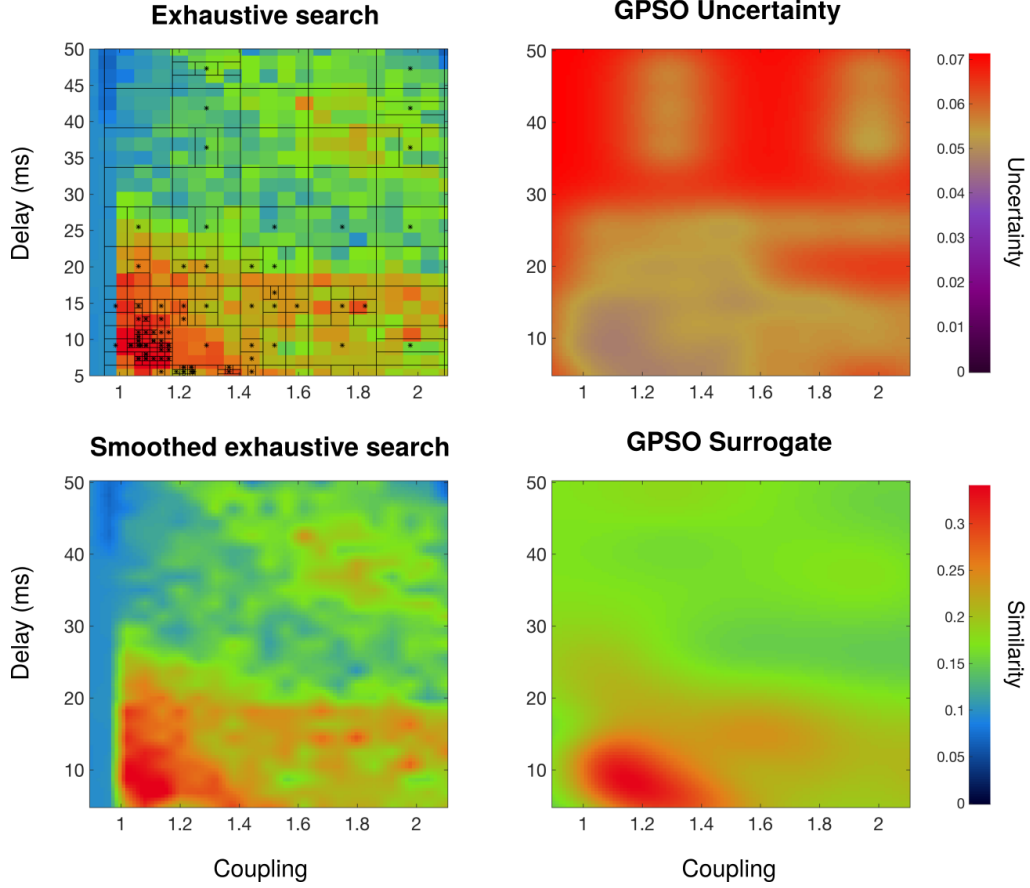
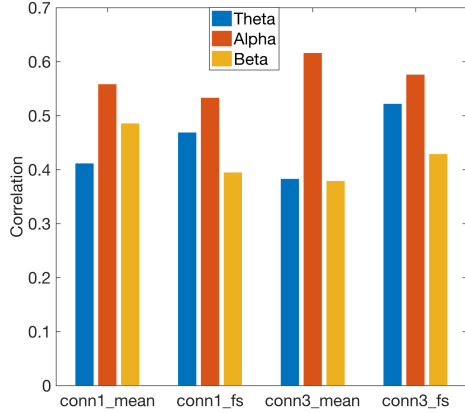


Figure 7: Exhaustive grid-search with 525 simulations, compared against GPSO with 100 simulations, controlling 2 parameters (average delay and relative coupling). The remaining parameters (see Tab. 2) were set to: $\widehat{P_e} = 0.85$, $h = 1$, $\tau = 10\text{ms}$, and we used the `conn1_mean` AC matrix to connect the network units. **Top-left:** exhaustive search (background image) and partition tree from the GPSO (black lines). Black asterisks indicate the samples evaluated during optimisation (see §2.1.3 for details about GP-based samples). Each pixel corresponds to a 63 sec simulation, analysed and compared with reference MEG data. The partition is refined in places where the objective function is higher, and the optimisation converged rapidly to the global optimum. **Bottom-row:** surrogate function (predicted mean) learned by GPSO, to be compared against the smoothed exhaustive search (ground-truth) on the left. **Top-right:** surrogate uncertainty (predicted st-dev.), driving the compromise between exploration and exploitation during optimisation.



	c1_mean	c1_fs	c3_mean	c3_fs
Obj	0.42	0.39	0.39	0.40
Cor	0.49	0.47	0.46	0.51

Figure 8: Best results obtained with the four AC matrices given in Fig. 5. The bar plot shows the correlation between simulated and reference FC matrices in theta, alpha and beta bands. The table reports the average correlation across bands, as well as the similarity score calculated with the objective function defined in §2.3.4. Without controlling for varying connectivity strength across frequency-bands, the results obtained with `conn3_fs` are better than those with `conn1_mean`, even though the corresponding FC matrices (see bottom-row in Fig. 9) are almost identical across bands. This illustrates the importance of choosing a suitable objective function.

matrices shown in Fig. 5. For each connectivity, an optimisation was run with 800 samples (*i.e.* evaluations of the objective functions), which took approximately 1.5 day to run on a computing cluster with four threads. In comparison, an exhaustive search run sequentially with just 20 values per dimension would take over 18 years to complete.

The five-dimensional results cannot be displayed as in the previous two-dimensional case; instead we summarise below key aspects of the analysis, illustrating the type of information made available by this new method.

A case for multi-criteria objective functions •. Defining the “goodness-of-fit” with resting-state electrophysiological data is a difficult task, especially given the time-constraints typically associated with LSBM optimisation. Here, we discuss

the benefits of including a penalty factor in the objective function, to ensure that the relative amounts of FC across frequency bands are similar in real and simulated data. It is best to have the main points of §2.3.4 in mind when reading this paragraph.

We illustrate our point in Fig. 8, where the best results obtained after optimisation with each of the four AC matrices are summarised and compared. Without the penalty term included in the objective function to control for the relative strength of connectivity across bands, the results obtained with `conn3_fs` connectivity would be better than those obtained with `conn1_mean` connectivity, despite the fact that the corresponding FC matrices (see bottom-row in Fig. 9) are almost identical across frequency bands, and only vary slightly in terms of connectivity scale. The FC matrices obtained with `conn1_mean` connectivity also had a better structural correspondence with the reference matrices (see top rows in Fig. 9), but this was only by chance; the penalty term did not favour this correspondence in any way. In fact, this is one of the weaknesses of the correlation coefficient itself, which does not take into account structural dependencies between the elements of the FC matrices (*i.e.* the connectivity *patterns*) when comparing them.

In brief, these results show that the inclusion of a penalty term controlling for relative strengths of FC across frequency bands was beneficial in our experiments, and suggest that multi-criteria objective function might in general be desirable in the context of LSBMs. Furthermore, the use of similarity metrics which explicitly account for structural correspondences between simulated and reference data may also enhance the quality of the optimisation.

Marginal parameter distributions reveal optimal value-ranges •. Looking at the distribution of parameter values for the best samples tells us about “preferred” values for each parameter; that is, parameter values for which the corresponding networks produce dynamical activity most similar to MEG resting-state data. Fig. 10 shows a comparison between the marginal parameter distributions computed independently for each of the four AC matrices. These distributions correspond to the

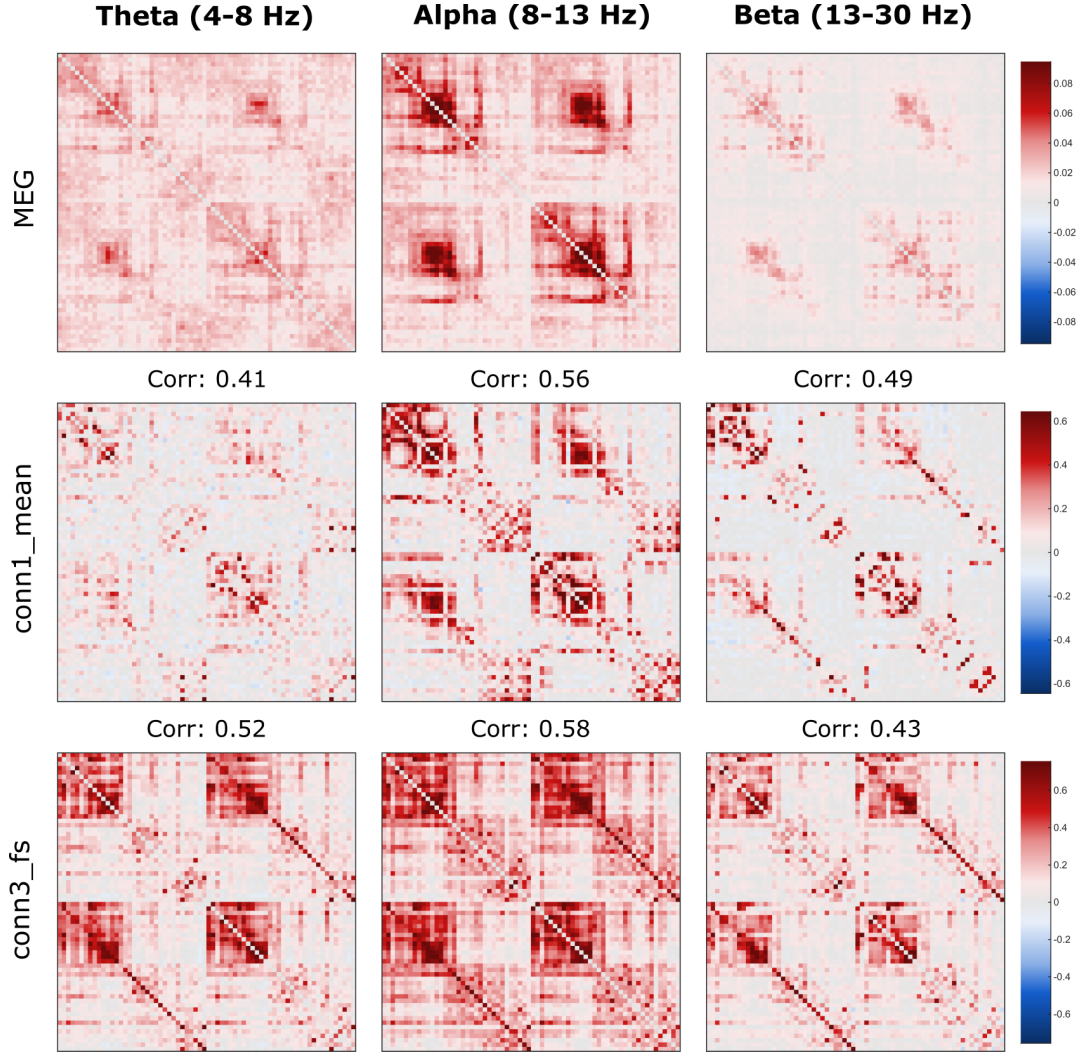


Figure 9: Comparison between simulated and reference FC matrices in theta, alpha and beta bands. Reference matrices are shown in the first row, followed by the best results obtained with connectivity **conn1_mean** (row 2), and the second best results obtained with **conn3_fs** (row 3). The correlation between each simulated FC matrix and the corresponding reference is indicated on top of the matrix. The FC patterns obtained with **conn1_mean** connectivity are strikingly similar to the reference, except in the frontal lobe (lower-right block in each quadrant). Note that although results obtained with **conn3_fs** achieved better correlations on average, they had a lower similarity score than the results obtained with **conn1_mean**, because their variation across bands was poor (see Fig. 8).

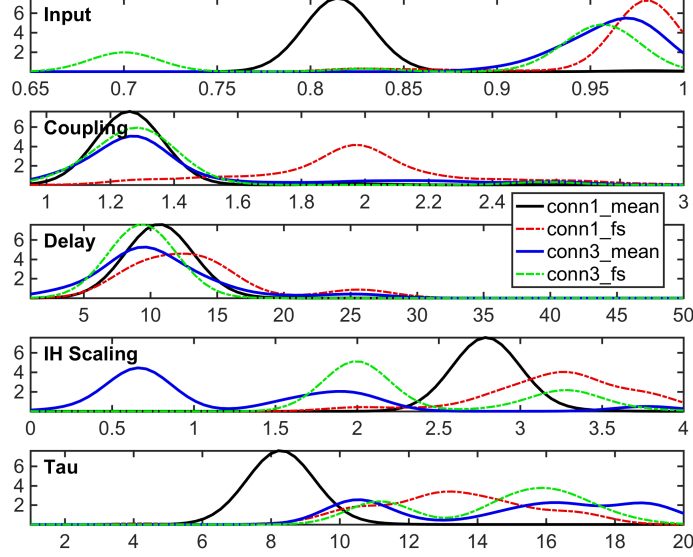


Figure 10: Marginal parameter distributions corresponding to the 90th percentile of all evaluated samples (*i.e.* using the objective function defined in §2.3.4), for each of the four AC matrices. Higher distribution values (y-axes) indicate ranges of parameters (x-axes) which were consistently associated with the best scores for a given AC matrix. **Input:** all but **conn1_mean** indicate that the excitatory input should be just below units’ oscillatory threshold. **Coupling:** all but **conn1_fs** indicate that coupling scale should be just above network oscillatory threshold. **Delay:** general consensus that average delay should be around 10ms. **Scaling:** no clear consensus, but all except **conn3_mean** indicate an upscale by a factor of 2 or more. **Tau:** **conn1_mean** centred around 8ms, and others above 10ms.

90th percentile of all evaluated samples (ranked according to their similarity score). The narrower the distributions, the stronger the preference for a specific parameter value. And the more overlap between distributions, the better the consensus across experiments with different connectivities.

We find a good consensus with regards to the first three parameters (input, coupling, delay), and in particular for the average network delay around 10ms, but the comparisons for the inter-hemispheric scaling h and characteristic time-constant τ are more mitigated. This is not surprising; the connectivity matrices control the interactions between the different brain regions, and structurally different networks should not be expected to agree on parameter values in general.

That being said, three out of the four AC matrices (all except **conn3_mean**) indicate clearly that the strength of inter-hemispheric connections should be increased at least two-fold. This is consistent with

the known bias for shorter connections in probabilistic tractography, but it is also remarkable to be able to estimate the amount of “missing” connectivity purely from simulations.

Finally, the results for the temporal parameters (average delay and time-constant) are somewhat surprising. We would not expect network delays to be lower on average than the characteristic time of variation within each brain region, because these delays are caused by axonal conduction over long distances, and local oscillations (caused by cycles of local excitation and inhibition) are not subject to propagation issues. This particular result might change with a more accurate estimation of the delays in our model (*e.g.* using tract-lengths from tractography instead of Euclidean distances), and may also be explained with further information about myelination information. Both of these enhancements will be explored in future work.

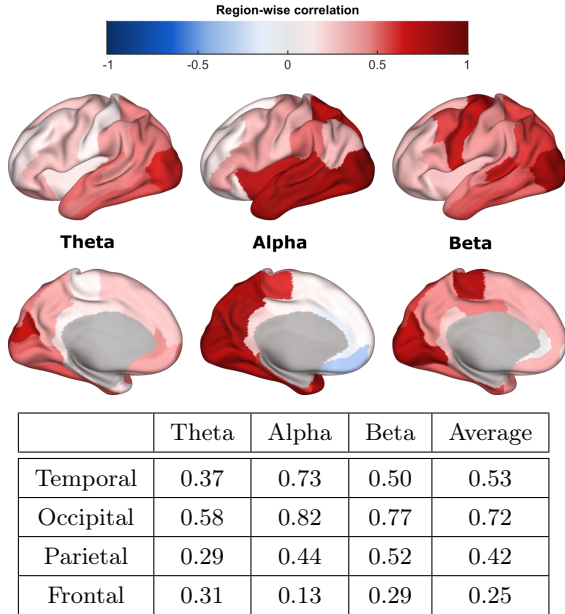


Figure 11: Region-wise correlation in each band, calculated between matching rows of simulated and reference FC matrices, for the best results obtained with `conn1_mean` connectivity. The average correlations within each lobe, for each band, are reported in the table below the surface illustrations. The correspondence between simulated and reference data is: very good in the occipital lobe; good in the temporal lobe, although driven mostly by the alpha band (>1.5 times better than other bands); consistently worse in the frontal lobe; and the average correspondence in the frontal+parietal lobes is twice as low as in the temporal+occipital lobes.

Conditional distributions reveal the local topography of the search space •. Here we take a deeper look at the best results obtained using `conn1_mean` connectivity. The optimal parameters correspond to a single point in the search space; to get an idea of the topography of the objective function around the optimum, we computed the conditional distributions of the GP surrogate on orthogonal slices going through that point. These slices are shown in Fig. 12.

A local maximum can be seen in the conditional surrogate coupling *vs.* input (row 2 column 1), which indicates that the objective function is not unimodal. Note that this is by no means a complete picture; for example, it is impossible to know about local optima located elsewhere in the search space based on this information only. Instead, the partition tree from GPSO (not shown for brevity)

can be used in combination with these conditional distribution, to identify local extrema and explore the topography of the search space around them.

Additionally, the marginally-weighted means and standard-deviations of the similarity scores obtained during optimisation are shown on the diagonal of Fig. 12, computed within each dimension across *all* samples in eleven bins covering the corresponding parameter range. These statistics are consistent with the parameter distributions previously shown in Fig. 10, although we previously only considered the 90th percentile of all samples.

Region-wise correlations reveal poor correspondence in the frontal lobe •. The correspondence between simulated and reference FC matrices shown in Fig. 9 can be explored further, by correlating each row of these matrices independently, in order to get a region-wise similarity score in each frequency-band. This comparison is illustrated in Fig. 11, by associating these correlations with a colour in each brain region and in each band. We find a very good correspondence across frequency bands in the temporal and occipital lobes, and systematically lower correlations in the frontal lobe, especially in the OFC.

The signal-to-noise ratio in the OFC is known to be rather poor in MEG [31], but the fact that the bad correspondence extends throughout the entire frontal lobe may relate to the work of [11], which introduced gradients of excitatory inputs in the frontal areas, in order to account for higher dendritic spine counts compared with primary sensory areas. This modification affects the frequency response of the frontal lobe, and therefore its properties of synchronisation within the whole-brain network, which could be the cause of the anti-correlation observed in the alpha band. Such lobe-specific treatment can be easily introduced in our model (similarly to the inter-hemispheric scaling) and will be explored in future work.

Whether gradients of excitatory inputs improve the correspondence with real data or not, however, it is remarkable to be able to point to such specific modelling aspects, with reasonable confidence that no other configuration of the current system could

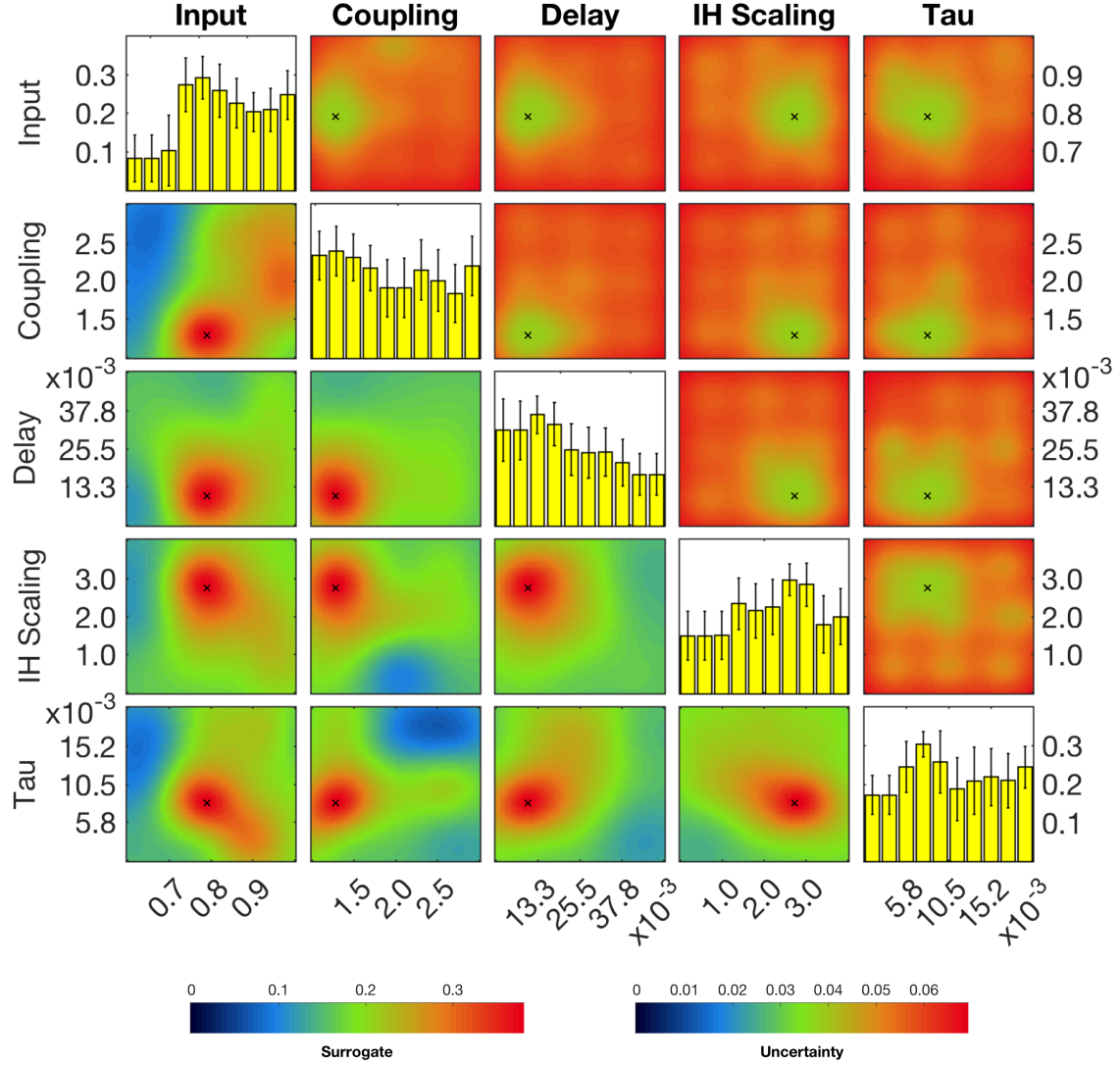


Figure 12: Conditional surrogate distributions (off-diagonal) and marginally weighted means and st-dev. (on-diagonal) around the best sample (black cross). These results correspond to the best experiment, using AC matrix `conn1_mean` (see Fig. 8). Note that y-axes at the top-left and bottom-right indicate similarity scores, whereas all other axes indicate parameter values. **Lower-triangle:** surrogate similarity (predicted mean) computed on orthogonal slices of the search space, going through the best sample for each pair of dimensions. **Upper-triangle:** associated surrogate uncertainty (predicted st-dev.) showing lowest uncertainty around the best sample, which is a good indicator of convergence. **Diagonal:** weighted mean and st-dev. of evaluated scores, calculated within each dimension across all samples. Higher bars indicate “preferred” values for the corresponding parameters (similar to the distributions shown in Fig. 10, but considering all samples).

yield a better result by tweaking the five parameters considered. These results tell us that a change to the *model* is required, and specifically one that will affect dynamics in the frontal areas. This type of information is invaluable, and demonstrates how GPSO can be used to inform modelling choices incrementally.

3.4. Discussion

Comparison with existing approaches • To our knowledge, no other work in the literature attempted the systematic optimisation of LSBMs with dozens of brain regions, in order to model fast-paced electrophysiological dynamics, and controlling five (or more) parameters. The computational and theoretical complexity of these models (due to their non-linearity, but also their size and the presence of delays), combined with the richness of electrophysiological data, calling for detailed objective functions leveraging the high temporal resolution, and the task of exploring parameter spaces as the number of dimensions increases (a.k.a. the curse of dimensionality), make the optimisation of LSBMs a truly difficult problem.

Our approach is different from the DCM method for network discovery [28], where the emphasis is put on inferring the *presence or absence* of structural connections, typically from fMRI data. For a given number of brain regions, this method considers all possible networks connecting these regions (that is, all possible combinations of edges), and proceeds to finding the network that is best supported by the observed data, as measured by the Bayesian model evidence, using generalised filtering [27]. Crucially, because it becomes rapidly impractical to list all possible networks as we consider more brain regions, let alone evaluate them, this method is made computationally efficient by exploiting the idea that it is sufficient to invert the fully-connected model in order to estimate the model evidence of any subnetwork. Furthermore, the method assumes that the posterior distribution over the connection strengths is multivariate Gaussian (the Laplace assumption); as such, it cannot represent accurately complex cost functions (*e.g.* with multiple modes, see Fig. 12), and in particular,

only considers a single extremum during optimisation, which makes it prone to converging towards local extrema depending on initialisation.

In our case, the network is taken as the AC matrix estimated from diffusion tractography, and the emphasis is put on the Bayesian optimisation method proposed, which can be used to infer model parameters (up to a dozen in practice) with arbitrary objective functions encoding the dynamical features of interest. This method is capable of handling the computational burden associated with LSBM simulations in practice, and the presence of local extrema in the objective function. It does so by building a smooth *surrogate* of the objective function using a Gaussian Process, which is refined as the optimisation progresses, and exploited in order to prioritise the exploration of areas in the parameter space that are either unknown, or promising given the available evidence.

Another approach [10, 23] proposed to eliminate the need to compute explicit solutions to the differential equations for several parameter values, in order to accelerate the task of inference. This method works backwards from the measured time-courses, linking to the model parameters by sampling the hyperparameters of a Gaussian Process encoding the relationship between state-variables and their derivatives. The authors demonstrated the performance of this approach in the case of systems with few state-variables and few time-points, assumed to be measured from experimental data; and extended it to the case of delay-differential equations, essentially by increasing the number of states considered at each timepoint. However, it is unlikely that this approach scales well to the case of systems with hundreds of *coupled* differential equations, with several dozens of unique delays, and for which the features relating to empirical measurements (*e.g.* functional connectivity) require tens of thousands of timepoints; sampling spaces that large, even if the cost of a single sample is low⁶, is simply impractical.

⁶The fact that our systems of equations are coupled with non-sparse interactions also means that the complexity of a single evaluation is still quadratic in the number of nodes.

Influence of local parameters •. There is no doubt that the parameters governing the local dynamics (e.g. given in Tab. 1) will, in general, affect the characteristics of the network activity; in fact, this is the premise of our study. The problem of systematically predicting network activity from local properties – the notorious *structure-function* problem – is currently unsolved, although this is an active area of research (see [57] for instance). The purpose of this paper is to propose a practical method allowing to search for a desired network behaviour in a reasonable time, by manipulating a relatively small number of parameters.

We demonstrated the efficiency of this method, and provided a typical analysis of the results obtained for the purpose of incremental modelling. Within this context, we selected only a handful of parameters, controlling key aspects of the dynamics; in particular, simultaneously shifting the decay times τ_e and τ_i of a unit, within a reasonable range of values, affects the range of oscillatory frequencies in response to network inputs (see Fig. 4, bottom-left).

It is also possible to control this range of frequencies by shifting τ_i alone (keeping τ_e fixed), but with the side-effect of altering the amplitude of oscillations as well (see middle plot in the same figure). Based on the physiological observation that inhibitory decay-times are typically longer than excitatory ones [58], it may be relevant to control these time-constants independently, and indeed preliminary experiments suggest that this can improve the spectral contents of large-scale network simulations, and leads to predictions of the average delay between regions around 20ms, instead of the 10ms predicted in our current results. Further investigation into the effects of unit parameters on the network dynamics will be the object of future work.

Influence of structural information •. It is clear that measuring functional properties at the whole-brain level ultimately depends on how the different brain regions are defined [53, 25]. In fact, defining cortical parcellations reliably most likely requires the integration of information across multiple modalities [29]. Furthermore, in the case of MEG, the “leakage” of spatial information, due to the ill-posed nature of source-reconstruction, adds

to the difficulty in delineating different brain regions [24].

Then, there is also the question of whether this parcellation can be applied indiscriminately to different subjects [35], although it is yet to be proven whether individual structural connectomes are better predictors of their own functional connectomes, than averaged ones. We have no definite answer to these questions, and indeed the effects of the anatomical parcellation, as well as potential predictions of subject-specific characteristics, will be the object of future work.

However, we would like to point out that several connectivity matrices (produced using different seeding and normalisation methods) were compared in the results presented, based on their ability to produce network dynamics of interest. In particular, the two best results obtained, using `conn1_mean` and `conn3_fs` AC matrices, indicate that inter-hemispheric connections should be between two and three times as strong (see Fig. 10). In other words, GPSO allowed us to assess *structure* (the AC matrix) from *function* (band-specific FC); this is an exciting perspective, and one with a different emphasis to previous work relating structure and function through biophysical models [56, 18].

Evaluating the performance of GPSO •. The ability of GPSO to converge to the global optimum, even in the presence of local extrema, was demonstrated in figures 2 and 7, both times in a two-dimensional context. We further demonstrate this ability in the case of a 5-dimensional space in appendix (for completeness, a comparison with a sequential Monte-Carlo method is also provided).

Despite its efficiency, however, there are a number of limitations currently associated with this method. **First**, it is not currently possible to systematically evaluate the convergence of the algorithm. This is mainly because at every iteration, multiple areas of the search space are being explored at multiple scales, which means that a lack of improvement in the best score obtained (typically a criterion for convergence) over several iterations is no guarantee that there will not be a substantial improvement at the next iteration. However, one can define several relevant termination criteria,

such as: the number of evaluations of the objective function (our case), the number of iterations, the depth of the partition tree, etc. **Second**, it is worth noting that because we only ever select those nodes with maximal UCB in the partition tree (see Fig. 1), areas of the search space with lower expected scores are the last to be evaluated at each level of the tree, and therefore the resolution of the surrogate is lower there. This is an intended consequence of prioritising exploration in places of high expected reward, but it also means that the surrogate will in general not be reliable when the objective function is low; such is the price to pay for efficiency, this is not primarily an exploration method. **Third**, it is currently not possible to define priors over the parameter ranges in order to initially bias the search towards regions of known interest. Note that this cannot be done via the mean function of the GP, because hyperparameters are revised at each iteration, and that making the prior insensitive to hyperparameters would also make it insensitive to evidence accumulated by simulations, effectively corrupting the objective function as a result. It could however be done by introducing a third type of point (currently either *evaluated*, or *GP-based*, see §2.1.3), which would not be updated following hyperparameter updates, but would need to be evaluated before proceeding to exploration in an arbitrary small neighbourhood. This would essentially be equivalent to introducing “ghost nodes” arbitrarily deep into the partition tree, waiting to be discovered by subdivision. **Finally**, although this is purely a technical limitation, it is worth mentioning that exact inference on the GP hyperparameters from the evaluated points becomes prohibitively slow beyond a few thousand samples⁷, which means that we cannot reasonably explore parameter spaces beyond 10 dimensions with exactness. Beyond this, resorting to approximate inference is possible, by selecting only a limited number of evaluated samples for training the GP; for instance, up to a certain depth in the partition tree, and randomly beyond that depth, up to a certain amount.

Objective function and parametrisation •. The objective function proposed in §2.3.4 combines a mea-

sure of the average correlation between empirical and simulated FC matrices, with a comparison between the relative amounts of connectivity strength across frequency bands. We illustrated in Fig. 8 the potential benefits of considering such multi-criteria objective functions, in the context of LSBM optimisation. In the long run however, it would be desirable to transition towards probabilistic models of functional connectivity, capturing not only the desired structural properties of the functional networks, but also the variability across subjects. The method proposed in this paper can readily be used with such models.

In addition to the choice of a suitable objective function, the parameters considered at the network level can significantly alter the characteristics of the simulated dynamics. For example, the heterogeneity of excitatory inputs across the network can give rise to rich spectral contents [11], and modifications to the delay structure (*e.g.* considering tract-lengths instead of Euclidean distances, and myelination) may lead to qualitatively different dynamics [43]. These aspects will be explored in future work.

4. Conclusion

The complexity of large-scale biophysical models (LSBMs) makes it difficult to affirm with confidence that a given system *cannot* produce dynamical activity with certain desired properties, and therefore to compare such systems. In this paper, we argued that for a given set of parameters, two models could be compared in terms of their performance with respect to an objective function (which encodes the desired dynamical behaviour) after optimisation. We presented a method allowing such optimisation to be carried out accurately, efficiently, and reliably, even in the presence of local extrema, and despite the computational burden associated with the simulations of LSBMs in practice.

Using this method to optimise simultaneously five parameters affecting both structural and functional aspects in delay-networks of 68 Wilson-Cowan oscillators, we were able to achieve the highest levels of expected correspondence with real resting-state

⁷Our implementation uses the GPML package [49]

MEG data across frequency bands, given the simulation time-lengths (see figures 9 and 6). Our results also suggest that inter-hemispheric anatomical connectivity, as estimated from diffusion tractography, may be underestimated by a factor 2 to 3, depending on the seeding and normalisation methods used. Furthermore, looking at region-wise correspondence in our best simulated results, we find systematically lower correlations in the frontal lobe, which indicates that further modelling work is required particularly in this area, perhaps in agreement with the work presented in [11].

Overall, these results suggest that Gaussian-Process Surrogate Optimisation (GPSO) is an effective method for exploring and comparing the capabilities of LSBMs. It enables the exploration of high-dimensional parameter spaces (compared with the current state-of-the-art), which offers unprecedented insights into the relationship between structure and function in biophysical models of brain activity.

5. Acknowledgements

We would like to thank the reviewers for their insightful comments.

We would also like to thank Matthew Brookes and his group for providing us with the MEG resting-state dataset of 28 healthy subjects. This data was collected as part of the Multi-modal Imaging Study in Psychosis (MISP) funded by grant MR/J01186X/1, and collected by Sian Robson and Emma Hall.

The Wellcome Centre for Integrative Neuroimaging is supported by core funding from the Wellcome Trust (203139/Z/16/Z).

J.H. is funded by the Oxford-Radcliffe DTC EPSRC Graduate Scholarship at University College, Oxford (EP/F500394/1). S.N.S. was supported in part by EPSRC (EP/L023067/1). M.W.W.'s research is supported by the NIHR Oxford Health Biomedical Research Centre, by the Wellcome Trust (106183/Z/14/Z), and the MRC UK MEG Partnership Grant (MR/K005464/1). S.J. is supported by the MRC UK (MR/L009013/1).

Appendices

Background on large-scale biophysical models

In the literature, the different large-scale modelling approaches can be grouped into three main categories:

- **Data-driven approaches:** these methods usually borrow from digital signal processing, and summarise key aspects of the observed dynamics (*e.g.* spectral profiles) with few parameters. For example, auto-regressive methods [34, 46] formulate explicit lagged dependencies between successive timepoints, typically in a multivariate fashion in order to capture structural interactions between distant brain regions. Although such approaches are designed to accurately reproduce the observed signals (often under linear assumptions), and can reveal structural dependencies in the data [45], they do not provide any insight into the underlying biophysical processes.
- **Neuronal-mass models:** these methods describe the average dynamics of large populations of densely connected neurons, with parametric systems of ordinary differential equations [60, 47]. In comparison with the previous data-driven approaches, these models are typically derived from first principles with a concern to remain faithful to the (relevant) underlying biophysics. Importantly, these models are inherently *local*, because they neglect the spatial dependency of the dynamics (*e.g.* due to axonal conduction delays) in order to work with functions of time only. However, large-scale models can be constructed, by considering *networks* of neuronal masses, with vertices summarising the local activity in different brain regions, and with edges representing (delayed) interactions between these regions.
- **Neural-field models:** these methods extend the previous mass-models, by considering brain activity as a diffusion process over the cortical surface [5, 13]. The temporal dynamics at any given point on the surface are derived from local equations, but the diffusion process allows nearby points to affect each

other, and the ensuing propagation across the surface typically leads to oscillatory activity through *travelling wave* mechanisms. Long-range interactions with delays can also be included by modifying the topology of the cortical surface, and multiple layers can be considered to model interactions between different types of neurons [14]. However, these models are theoretically and computationally complex compared to neuronal masses, and less developed to date. Furthermore, although quantitative differences have been demonstrated [48], it is unclear whether this added complexity is *required* in order to produce dynamics of interest in large-scale models.

Additionally, it is worth noting that large-scale *spiking* models considering very large networks of individual neurons have been attempted [38], but their overwhelming complexity precludes any practical exploration of their capabilities.

In this paper, we focused on the use of neuronal-mass models, as a reasonable compromise between complexity and biophysical pertinence. The general structure of these models is best described as a discrete **network**; in particular, the different brain regions are associated with network **units**, which may themselves be composed of several **nodes** associated with different local populations of neurons.

Evaluation of GPSO in dimension 5

Below, we assess the ability of GPSO to converge to the global optimum in the case of a five-dimensional search-space. For reference, we compare the performance achieved to that of a sequential Monte-Carlo method (particle filter). We emphasize, however, that the two methods differ fundamentally in their approach, and that this comparison is not intended as a competition; random sampling methods are built around the property of ergodicity (*i.e.* the probability of sampling any open subspace is positive, hence any region will *eventually* be sampled), whereas space-partitioning methods like GPSO implement a multi-scale “divide-and-conquer” philosophy, relying on the smoothness of the objective function. Therefore, as noted previously in §2.1,

random sampling methods are undesirable in practice in the case of expensive objective functions, because they do not attempt to minimise the number of function evaluations, and yield variable results for small sample sizes.

In order to assess the convergence of GPSO fairly and reliably, we constructed *ten* objective functions as mixtures of (isotropic) Gaussians, with 5 modes (or peaks) each, restricted to the space $(0, 1)^5$. We imposed that the modes be far apart from each other, mainly to ensure that the global optimum would be one of the peaks (allowing multiple peaks to merge makes it difficult to analytically locate the global optimum).

For each peak of each mixture, the width σ and amplitude A were sampled randomly, respectively in $(0.1, 0.2)$ and $(1, 5)$. Then, the location μ was sampled randomly within $(\sigma, 1 - \sigma)^5$, and the peak was *rejected* if either:

- the value of the mixture considering previous peaks only was greater than $V = 0.3$;
- or the closest previous peak was at a distance closer than:

$$\sigma \sqrt{2 \log \left(\frac{A}{V} \right)}$$

Once the peaks were chosen for each mixture, GPSO was run for each mixture with 800 samples, using the same parameters given in Tab. 3. The performance of each run was measured in terms of:

- whether the global optimum was found;
- if so, with the closest distance to the optimum;
- if not, with the distance to the closest peak.

We found that GPSO converged to the global optimum nine out of ten times (despite the presence of local extrema), and the distance to the optimum in these cases was 0.0096 ± 0.0062 . The one time it converged to a local maximum instead, the distance to the closest peak was 0.013, and the difference in height between this peak (4.34) and the global maximum (4.90) was 0.56.

This performance was compared to a sequential Monte-Carlo sampling scheme, namely *particle-filter* optimisation [21, 42]. This scheme proceeded over eight cycles, each with 100 samples (*i.e.* 800 samples in total, as previously with GPSO), as follows:

- the first 100 samples were selected uniformly randomly;
- at each cycle, the last third of the samples were resampled uniformly, and the best two-thirds were resampled following an SIR procedure (sequential importance resampling), using an isotropic Gaussian distribution with standard-deviation 0.1.

Due to the stochastic nature of this procedure, we repeated the optimisation ten times for each mixture function, and estimated the success rate across these ten trials, based on whether the particle with the highest score (across all 800) was closest to the highest peak. Overall, the success-rate was of 69%; the distance to the global optimum in these cases was 0.085 ± 0.027 ; and otherwise, the distance to the closest optimum was 0.080 ± 0.028 .

It is worth noting that the average time GPSO required in order to carry out this optimisation was 11.4 min, whereas the particle sampling scheme completed on average within 10 ms. This illustrates the fact that GPSO is only valuable in the case of *costly* objective functions, for which the time required to carry out the optimisation is negligible compared to the time required to evaluate the various samples.

References

- [1] R. G. Abeysuriya, J. Hadida, S. N. Sotiropoulos, S. Jbabdi, R. Becker, B. A. Hunt, M. J. Brookes, and M. W. Woolrich. A biophysical model of dynamic balancing of excitation and inhibition in fast oscillatory large-scale networks. (In submission), 2017.
- [2] P. Auer, N. Cesa-Bianchi, and P. Fischer. Finite-time analysis of the multiarmed bandit problem. *Machine Learning*, 47(2/3):235–256, 2002.
- [3] T. E. J. Behrens, H. J. Berg, S. Jbabdi, M. F. S. Rushworth, and M. Woolrich. Probabilistic diffusion tractography with multiple fibre orientations: What can we gain? *NeuroImage*, 34(1):144–155, 2007.
- [4] M. Breakspear. Dynamic models of large-scale brain activity. *Nature Neuroscience*, 20(3):340–352, feb 2017.
- [5] P. C. Bressloff. Spatially periodic modulation of cortical patterns by long-range horizontal connections. *Physica D: Nonlinear Phenomena*, 185(3-4):131–157, nov 2003.
- [6] E. Brochu, V. M. Cora, and N. de Freitas. A tutorial on bayesian optimization of expensive cost functions, with application to active user modeling and hierarchical reinforcement learning. *ArXiv*, page 49, dec 2010.
- [7] M. J. Brookes, E. L. Hall, S. E. Robson, D. Price, L. Palaniyappan, E. B. Liddle, P. F. Liddle, S. E. Robinson, and P. G. Morris. Complexity measures in magnetoencephalography: Measuring "disorder" in schizophrenia. *PLOS ONE*, 10(4):e0120991, apr 2015.
- [8] S. Bubeck and N. Cesa-Bianchi. Regret analysis of stochastic and nonstochastic multi-armed bandit problems. *arXiv.org*, cs.LG:138, apr 2012.
- [9] G. Buzsáki, C. a. Anastassiou, and C. Koch. The origin of extracellular fields and currents — eeg, ecog, lfp and spikes. *Nature Reviews Neuroscience*, 13(6):407–420, may 2012.
- [10] B. Calderhead, M. Girolami, and N. D. Lawrence. Accelerating bayesian inference over nonlinear differential equations with gaussian processes. *Advances in Neural Information Processing Systems 21*, pages 217–224, 2009.
- [11] R. Chaudhuri, K. Knoblauch, M.-A. Gariel, H. Kennedy, and X.-J. Wang. A large-scale circuit mechanism for hierarchical dynamical processing in the primate cortex. *Neuron*, 88(2):419–431, oct 2015.
- [12] G. Colclough, M. Brookes, S. Smith, and M. Woolrich. A symmetric multivariate leakage correction for meg connectomes. *NeuroImage*, 117:439–448, aug 2015.
- [13] S. Coombes. Large-scale neural dynamics: Simple and complex. *NeuroImage*, 52(3):731–739, sep 2010.
- [14] S. Coombes, P. beim Graben, R. Potthast, and J. Wright. *Neural Fields*. Springer Berlin Heidelberg, Berlin, Heidelberg, 2014.

- [15] N. de Freitas, A. Smola, and M. Zoghi. Exponential regret bounds for gaussian process bandits with deterministic observations. *Proceedings of the 29th International Conference on Machine Learning (ICML-12)*, pages 1743–1750, jun 2012.
- [16] G. Deco, V. Jirsa, A. R. McIntosh, O. Sporns, and R. Kotter. Key role of coupling, delay, and noise in resting brain fluctuations. *Proceedings of the National Academy of Sciences*, 106(25):10302–10307, jun 2009.
- [17] G. Deco, V. K. Jirsa, P. A. Robinson, M. Breakspear, and K. Friston. The dynamic brain: From spiking neurons to neural masses and cortical fields. *PLoS Computational Biology*, 4(8), 2008.
- [18] G. Deco, A. R. McIntosh, K. Shen, R. M. Hutchison, R. S. Menon, S. Everling, P. Hagmann, and V. K. Jirsa. Identification of optimal structural connectivity using functional connectivity and neural modeling. *Journal of Neuroscience*, 34(23):7910–7916, jun 2014.
- [19] G. Deco, A. Ponce-Alvarez, D. Mantini, G. L. Romani, P. Hagmann, and M. Corbetta. Resting-state functional connectivity emerges from structurally and dynamically shaped slow linear fluctuations. *Journal of Neuroscience*, 33(27):11239–11252, jul 2013.
- [20] R. S. Desikan, F. Ségonne, B. Fischl, B. T. Quinn, B. C. Dickerson, D. Blacker, R. L. Buckner, A. M. Dale, R. P. Maguire, B. T. Hyman, M. S. Albert, and R. J. Killiany. An automated labeling system for subdividing the human cerebral cortex on mri scans into gyral based regions of interest. *NeuroImage*, 31(3):968–980, jul 2006.
- [21] P. Djuric, J. Kotecha, J. Zhang, Y. Huang, T. Ghirmai, M. Bugallo, and J. Miguez. Particle filtering. *IEEE Signal Processing Magazine*, 20(5):19–38, sep 2003.
- [22] C. J. Donahue, S. N. Sotiropoulos, S. Jbabdi, M. Hernandez-Fernandez, T. E. Behrens, T. B. Dyrby, T. Coalson, H. Kennedy, K. Knoblauch, D. C. Van Essen, and M. F. Glasser. Using diffusion tractography to predict cortical connection strength and distance: A quantitative comparison with tracers in the monkey. *Journal of Neuroscience*, 36(25):6758–6770, jun 2016.
- [23] F. Dondelinger and D. Husmeier. Ode parameter inference using adaptive gradient matching with gaussian processes. *Sixteenth International Conference on Artificial Intelligence and Statistics*, 31:13, 2013.
- [24] S.-R. Farahibozorg, R. N. Henson, and O. Hauk. Adaptive cortical parcellations for source reconstructed eeg/meg connectomes. *NeuroImage*, sep 2017.
- [25] A. Fornito, A. Zalesky, and M. Breakspear. Graph analysis of the human connectome: promise, progress, and pitfalls. *NeuroImage*, 80:426–44, oct 2013.
- [26] K. Friston. Functional integration and inference in the brain. *Progress in Neurobiology*, 68(2):113–143, oct 2002.
- [27] K. Friston, K. Stephan, B. Li, and J. Daunizeau. Generalised filtering. *Mathematical Problems in Engineering*, 2010:1–34, 2010.
- [28] K. J. Friston, B. Li, J. Daunizeau, and K. E. Stephan. Network discovery with dcm. *NeuroImage*, 56(3):1202–1221, jun 2011.
- [29] M. F. Glasser, T. S. Coalson, E. C. Robinson, C. D. Hacker, J. Harwell, E. Yacoub, K. Ugurbil, J. Andersson, C. F. Beckmann, M. Jenkinson, S. M. Smith, and D. C. Van Essen. A multi-modal parcellation of human cerebral cortex. *Nature*, 536(7615):171–8, aug 2016.
- [30] M. F. Glasser, S. N. Sotiropoulos, J. A. Wilson, T. S. Coalson, B. Fischl, J. L. Andersson, J. Xu, S. Jbabdi, M. Webster, J. R. Polimeni, D. C. Van Essen, and M. Jenkinson. The minimal preprocessing pipelines for the human connectome project. *NeuroImage*, 80(6):105–124, oct 2013.
- [31] D. M. Goldenholz, S. P. Ahlfors, M. S. Hämäläinen, D. Sharon, M. Ishitobi, L. M. Vaina, and S. M. Stuffelbeim. Mapping the signal-to-noise-ratios of cortical sources in magnetoencephalography and electroencephalography. *Human Brain Mapping*, 30(4):1077–1086, apr 2009.
- [32] M. D. Greicius, K. Supekar, V. Menon, and R. F. Dougherty. Resting-state functional connectivity reflects structural connectivity in the default mode network. *Cerebral cortex (New York, N.Y. : 1991)*, 19(1):72–8, jan 2009.
- [33] E. Hairer and G. Wanner. *Solving Ordinary Differential Equations II*. Springer, Berlin, 1996.
- [34] L. Harrison, W. Penny, and K. Friston. Multivariate autoregressive modeling of fmri time series. *NeuroImage*, 19(4):1477–1491, aug 2003.
- [35] S. J. Harrison, M. W. Woolrich, E. C. Robinson, M. F. Glasser, C. F. Beckmann, M. Jenkinson, and S. M. Smith. Large-scale probabilistic functional modes from resting state fmri. *NeuroImage*, 109:217–31, apr 2015.
- [36] M. Hernández, G. D. Guerrero, J. M. Cecilia, J. M. García, A. Inuggi, S. Jbabdi, T. E. J. Behrens, and S. N. Sotiropoulos. Accelerating fibre orientation estimation from diffusion weighted magnetic resonance imaging using gpus. *PLoS ONE*, 8(4):e61892, apr 2013.
- [37] C. J. Honey, O. Sporns, L. Cammoun, X. Gigandet, J. P. Thiran, R. Meuli, and P. Hagmann. Predicting human resting-state functional connectivity from structural connectivity. *Proceedings of the National Academy of Sciences*, 106(6):2035–2040, feb 2009.
- [38] E. M. Izhikevich and G. M. Edelman. Large-scale model of mammalian thalamocortical systems. *Proceedings of the National Academy of Sciences of the United States of America*, 105(9):3593–3598, 2008.

- [39] S. Jbabdi, S. N. Sotiropoulos, S. N. Haber, D. C. Van Essen, and T. E. Behrens. Measuring macroscopic brain connections in vivo. *Nature Neuroscience*, 18(11):1546–1555, oct 2015.
- [40] S. Jbabdi, S. N. Sotiropoulos, A. M. Savio, M. Graña, and T. E. J. Behrens. Model-based analysis of multishell diffusion mr data for tractography: How to get over fitting problems. *Magnetic Resonance in Medicine*, 68(6):1846–1855, dec 2012.
- [41] K. Kawaguchi, L. P. Kaelbling, and T. Lozano-Pérez. Bayesian optimization with exponential convergence. *Neural Information Processing Systems*, pages 1–9, apr 2016.
- [42] B. Liu, S. Cheng, and Y. Shi. Particle filter optimization: A brief introduction. In *Studies in Computational Intelligence*, volume 248, pages 95–104. 2016.
- [43] L. Lücken, J. P. Pade, and K. Knauer. Classification of coupled dynamical systems with multiple delays: Finding the minimal number of delays. *SIAM Journal on Applied Dynamical Systems*, 14(1):286–304, jan 2015.
- [44] J. Meier, P. Tewarie, A. Hillebrand, L. Douw, B. W. van Dijk, S. M. Stufflebeam, and P. Van Mieghem. A mapping between structural and functional brain networks. *Brain Connectivity*, 6(4):298–311, may 2016.
- [45] A. Messe, H. Benali, and G. Marrelec. Relating structural and functional connectivity in mri: A simple model for a complex brain. *IEEE transactions on medical imaging*, 0062(c):1–11, 2014.
- [46] G. Michalareas, J. M. Schoffelen, G. Paterson, and J. Gross. Investigating causality between interacting brain areas with multivariate autoregressive models of meg sensor data. *Human Brain Mapping*, 34(4):890–913, 2013.
- [47] D. Pinotsis, P. Robinson, P. beim Graben, and K. Friston. Neural masses and fields: modeling the dynamics of brain activity. *Frontiers in Computational Neuroscience*, 8(November):1–3, nov 2014.
- [48] D. a. Pinotsis, M. Leite, and K. J. Friston. On conductance-based neural field models. *Frontiers in computational neuroscience*, 7(November):158, 2013.
- [49] C. E. Rasmussen and C. K. I. Williams. *Gaussian Processes for Machine Learning*. Adaptive Computation and Machine Learning. MIT Press, Cambridge, MA, USA, jan 2006.
- [50] S. E. Robson, M. J. Brookes, E. L. Hall, L. Palaniyappan, J. Kumar, M. Skelton, N. G. Christodoulou, A. Qureshi, F. Jan, M. Z. Katshu, E. B. Liddle, P. F. Liddle, and P. G. Morris. Abnormal visuomotor processing in schizophrenia. *NeuroImage: Clinical*, 12:869–878, feb 2016.
- [51] B. L. Sabatini and W. G. Regehr. Timing of synaptic transmission. *Annual Review of Physiology*, 61(1):521–542, mar 1999.
- [52] P. Sanz-Leon, S. A. Knock, A. Spiegler, and V. K. Jirsa. Mathematical framework for large-scale brain network modeling in the virtual brain. *NeuroImage*, 111:385–430, 2015.
- [53] S. M. Smith, K. L. Miller, G. Salimi-Khorshidi, M. Webster, C. F. Beckmann, T. E. Nichols, J. D. Ramsey, and M. W. Woolrich. Network modelling methods for fmri. *NeuroImage*, 54(2):875–91, jan 2011.
- [54] S. N. Sotiropoulos, S. Jbabdi, J. Xu, J. L. Andersson, S. Moeller, E. J. Auerbach, M. F. Glasser, M. Hernandez, G. Sapiro, M. Jenkinson, D. A. Feinberg, E. Yacoub, C. Lenglet, D. C. Van Essen, K. Ugurbil, and T. E. Behrens. Advances in diffusion mri acquisition and processing in the human connectome project. *NeuroImage*, 80:125–143, oct 2013.
- [55] S. N. Sotiropoulos and A. Zalesky. Building connectomes using diffusion mri: why, how and but. *NMR in Biomedicine*, (April):e3752, jun 2017.
- [56] K. E. Stephan, M. Tittgemeyer, T. R. Knösche, R. J. Moran, and K. J. Friston. Tractography-based priors for dynamic causal models. *NeuroImage*, 47(4):1628–1638, oct 2009.
- [57] J. Stroud, M. Barahona, and T. Pereira. Dynamics of cluster synchronisation in modular networks: Implications for structural and functional networks. pages 107–130. 2015.
- [58] S. J. Tripathy, J. Savitskaya, S. D. Burton, N. N. Urban, and R. C. Gerkin. Neuroelectro: a window to the world’s neuron electrophysiology data. *Frontiers in Neuroinformatics*, 8(April):40, apr 2014.
- [59] D. Van Essen, K. Ugurbil, E. Auerbach, D. Barch, T. Behrens, R. Bucholz, A. Chang, L. Chen, M. Corbetta, S. Curtiss, S. Della Penna, D. Feinberg, M. Glasser, N. Harel, A. Heath, L. Larson-Prior, D. Marcus, G. Michalareas, S. Moeller, R. Oostenveld, S. Petersen, F. Prior, B. Schlaggar, S. Smith, A. Snyder, J. Xu, and E. Yacoub. The human connectome project: A data acquisition perspective. *NeuroImage*, 62(4):2222–2231, oct 2012.
- [60] T. P. Vogels, K. Rajan, and L. Abbott. Neural network dynamics. *Annual Review of Neuroscience*, 28(1):357–376, 2005.
- [61] H. R. Wilson and J. D. Cowan. Excitatory and inhibitory interactions in localized populations of model neurons. *Biophysical Journal*, 12(1):1–24, jan 1972.
- [62] M. W. Woolrich and K. E. Stephan. Biophysical network models and the human connectome. *NeuroImage*, 80:330–8, oct 2013.